The Astrophysical Journal, 983:152 (19pp), 2025 April 20 https://doi.org/10.3847/1538-4357/adbbdc

BEACON: JWST NIRCam Pure-parallel Imaging Survey. I. Survey Design and Initial Results

Takahiro Morishita[1,32], Charlotte A. Mason[2,3,32], Kimi C. Kreilgaard[2,3], Michele Trenti[4,5], Tommaso Treu[6], Benedetta Vulcani[7], Yechi Zhang[1], Abdurro'uf[8,9], Anahita Alavi[10], Hakim Atek[11], Yannick Bahé[12], Maruša Bradač[13,14], Larry D. Bradley[9], Andrew J. Bunker[15], Dan Coe[8,9,16], James Colbert[17], Viola Gelli[2,3], Matthew J. Hayes[18], Tucker Jones[19], Tadayuki Kodama[20], Nicha Leethochawalit[21], Zhaoran Liu[20], Matthew A. Malkan[22], Vihang Mehta[17], Benjamin Metha[4,5], Andrew B. Newman[23], Marc Rafelski[24,25], Guido Roberts-Borsani[26], Michael J. Rutkowski[27], Claudia Scarlata[28], Massimo Stiavelli[24], Ryo A. Sutanto[20], Kosuke Takahashi[20], Harry I. Teplitz[10], and Xin Wang[29,30,31]

[1] IPAC, California Institute of Technology, MC 314-6, 1200 E. California Boulevard, Pasadena, CA 91125, USA; takahiro@ipac.caltech.edu
[2] Cosmic Dawn Center (DAWN), Denmark; charlotte.mason@nbi.ku.dk
[3] Niels Bohr Institute, University of Copenhagen, Jagtvej 128, DK-2200 Copenhagen N, Denmark
[4] School of Physics, University of Melbourne, Parkville 3010, VIC, Australia
[5] ARC Centre of Excellence for All Sky Astrophysics in 3 Dimensions (ASTRO 3D), Australia
[6] Department of Physics and Astronomy, University of California, Los Angeles, 430 Portola Plaza, Los Angeles, CA 90095, USA
[7] INAF Osservatorio Astronomico di Padova, vicolo dell'Osservatorio 5, 35122 Padova, Italy
[8] Department of Physics and Astronomy, The Johns Hopkins University, 3400 N Charles St., Baltimore, MD 21218, USA
[9] Space Telescope Science Institute (STScI), 3700 San Martin Drive, Baltimore, MD 21218, USA
[10] IPAC, Mail Code 314-6, California Institute of Technology, 1200 E. California Boulevard, Pasadena, CA 91125, USA
[11] Institut d'Astrophysique de Paris, CNRS, Sorbonne Université, 98bis Boulevard Arago, 75014, Paris, France
[12] Institute of Physics, Laboratory of Astrophysics, Ecole Polytechnique Fédérale de Lausanne (EPFL), Observatoire de Sauverny, CH-1290 Versoix, Switzerland
[13] University of Ljubljana, Department of Mathematics and Physics, Jadranska ulica 19, SI-1000 Ljubljana, Slovenia
[14] Department of Physics and Astronomy, University of California Davis, 1 Shields Avenue, Davis, CA 95616, USA
[15] Department of Physics, University of Oxford, Denys Wilkinson Building, Keble Road, Oxford OX1 3RH, UK
[16] Association of Universities for Research in Astronomy (AURA), Inc. for the European Space Agency (ESA), USA
[17] IPAC, California Institute of Technology, 1200 E. California Boulevard, Pasadena, CA 91125, USA
[18] Stockholm University, Department of Astronomy and Oskar Klein Centre for Cosmoparticle Physics, AlbaNova University Centre, SE-10691, Stockholm, Sweden
[19] University of California, Davis, Department of Physics and Astronomy, One Shields Avenue, Davis, CA 95616, USA
[20] Astronomical Institute, Tohoku University, 6-3 Aramaki, Aoba-ku, Sendai 980-8578, Japan
[21] National Astronomical Research Institute of Thailand (NARIT), Mae Rim, Chiang Mai, 50180, Thailand
[22] University of California, Los Angeles, Department of Physics and Astronomy, 430 Portola Plaza, Los Angeles, CA 90095, USA
[23] Observatories of the Carnegie Institution for Science, Pasadena, CA, USA
[24] Space Telescope Science Institute, 3700 San Martin Drive, Baltimore, MD 21218, USA
[25] Department of Physics and Astronomy, Johns Hopkins University, Baltimore, MD 21218, USA
[26] Department of Astronomy, University of Geneva, Chemin Pegasi 51, 1290 Versoix, Switzerland
[27] Minnesota State University, Mankato, Department of Physics and Astronomy, 141 Trafton Science Center N, Mankato, MN 56001, USA
[28] University of Minnesota, Twin Cities, 116 Church St SE, Minneapolis, MN 55455, USA
[29] School of Astronomy and Space Science, University of Chinese Academy of Sciences (UCAS), Beijing 100049, People's Republic of China
[30] National Astronomical Observatories, Chinese Academy of Sciences, Beijing 100101, People's Republic of China
[31] Institute for Frontiers in Astronomy and Astrophysics, Beijing Normal University, Beijing 102206, People's Republic of China
Received 2024 December 4; revised 2025 February 14; accepted 2025 February 28; published 2025 April 16

Abstract

We introduce the Bias-free Extragalactic Analysis for Cosmic Origins with NIRCam (BEACON) survey, a JWST Cycle 2 program allocated up to 600 *pure-parallel* hours of observations. BEACON explores high-latitude areas of the sky with JWST/NIRCam over ∼100 independent sight lines, totaling ∼0.3 deg^2, reaching a median F444W depth of ≈28.2 AB mag (5σ). Based on existing JWST observations in legacy fields, we estimate that BEACON will photometrically identify 25–150 galaxies at $z > 10$ and 500–1000 at $z \sim 7$–10 uniquely enabled by an efficient multiple filter configuration spanning 0.9–5.0 μm. The expected sample size of $z > 10$ galaxies will allow us to obtain robust number density estimates and to discriminate between different models of early star formation. In this paper, we present an overview of the survey design and initial results using the first 19 fields. We present 129 galaxy candidates at $z \gtrsim 7$ identified in those fields, including 11 galaxies at $z \gtrsim 10$ and several UV-luminous ($M_{\rm UV} < -21$ mag) galaxies at $z \sim 8$. The number densities of $z < 13$ galaxies inferred from the initial fields are overall consistent with those in the literature. Despite reaching a considerably large volume (∼10^5 Mpc^3), however, we find no galaxy candidates at $z > 13$, providing us with a complimentary insight into early galaxy evolution with minimal cosmic variance. We publish imaging and catalog data products for these initial fields. Upon survey

[32] These authors equally contributed to this work.

completion, all BEACON data will be coherently processed and distributed to the community along with catalogs for redshift and other physical quantities.

Unified Astronomy Thesaurus concepts: Galaxies (573); Reionization (1383); High-redshift galaxies (734)

1. Introduction

Space telescopes have been essential for understanding galaxy formation and evolution, with the Hubble Space Telescope (HST) in particular progressively extending our frontiers from the pioneering Hubble Deep Field at redshift $z \sim 4$ (lookback time ~ 12 Gyr; e.g., P. Madau et al. 1996), to more recent discoveries of galaxies in the epoch of reionization ($z \sim 6$–10, lookback time > 13 Gyr; e.g., A. J. Bunker et al. 2004; R. J. Bouwens et al. 2010, 2015; A. J. Bunker et al. 2010; P. A. Oesch et al. 2010, 2018; R. S. Ellis et al. 2013; M. Ishigaki et al. 2018). However, even with the deepest HST and Spitzer data, key questions remained unanswered: When and how did the first sources of light form? How was intergalactic hydrogen reionized? How are galaxy mass and structure acquired across cosmic time? The James Webb Space Telescope (JWST) was designed to address these fundamental questions.

The advent of JWST marked a watershed moment. It extended the frontier of galaxy detection to the first 400 million years after the Big Bang ($z \gtrsim 11$) during the initial stages of reionization, finding a tantalizingly high abundance of bright, potentially massive galaxy candidates, unanticipated by theoretical models (e.g., M. Castellano et al. 2022; E. Curtis-Lake et al. 2023; C. T. Donnan et al. 2023; S. L. Finkelstein et al. 2022; R. P. Naidu et al. 2022; S. Carniani et al. 2024). Furthermore, the observed number of massive quenched galaxies exceeds expectations across $z \sim 3$–9 (A. C. Carnall et al. 2023; K. Glazebrook et al. 2024; A. de Graaff et al. 2025; T. Nanayakkara et al. 2024), a number of low-luminosity and dusty quasars (Y. Harikane et al. 2023c; D. D. Kocevski et al. 2023; J. Matthee et al. 2024; M. Onoue et al. 2023) or active galactic nuclei (AGN)–galaxy complexes (J. E. Greene et al. 2024; R. L. Larson et al. 2023a; J. Scholtz et al. 2024; H. Übler et al. 2023) have been revealed, and some galaxies seem to already have (proto)disk structures (L. Ferreira et al. 2022; Y. Fudamoto et al. 2022; C. J. Conselice et al. 2024; M. Xiao et al. 2024). However, these early results have come from just a handful of small public legacy fields (e.g., N. J. Adams et al. 2024; S. L. Finkelstein et al. 2024; D. J. McLeod et al. 2024), leaving open the question of how representative they are of the entire early Universe. More recently, C. J. Willott et al. (2024) extended the analysis to five new fields and found no luminous galaxies at $z > 10$, a stark contrast to the early studies.

Luminous galaxies are rare ($<10^{-5}$ Mpc^{-3} for $M_{\rm UV} < -21$ at $z > 7$; R. J. Bouwens et al. 2015) and inevitably subject to cosmic variance (R. S. Somerville et al. 2004; M. Trenti & M. Stiavelli 2008; B. E. Robertson 2010; A. K. Bhowmick et al. 2020; C. Kragh Jespersen et al. 2025). A good example of strong cosmic variance is that G. W. Roberts-Borsani et al. (2016) discovered three bright ($m_{\rm AB} < 26$) $z > 7$ galaxy candidates in just one of the five CANDELS fields, the Extended Groth Strip (EGS) field, whereas only one comparably bright candidate was detected from the other four fields. Subsequent follow-up in EGS with HST, ground-based spectroscopy, and JWST has revealed that this region appears overdense at $z \sim 7$–9, and contains the majority of Lyα emission detected across all legacy fields at $z > 7$, likely pointing to a site of significant star formation that reionized early (D. P. Stark et al. 2017; V. Tilvi et al. 2020; I. Jung et al. 2022; R. L. Larson et al. 2022; Z. Chen et al. 2023; M. Tang et al. 2023; L. Whitler et al. 2023). Such examples clearly demonstrate that a survey of many sightlines, as a supplement to legacy-type surveys with a small number of sightlines, is necessary for unbiased measurements in the early Universe under the presence of strong cosmic variance (see also Section 2.1).

Pure-parallel observations offer an ideal opportunity to meet this requirement. While the primary instrument is in operation, a secondary instrument can be used in parallel to observe a field a few arcminutes away. Since the coordinates of the pure-parallel field cannot be specified, pure-parallel opportunities are often used to identify objects without any prior knowledge, minimizing the effects of cosmic variance (Figure 1; also H. Atek et al. 2011; A. C. Trapp et al. 2023).

Starting in 2010, there have been several such HST pure-parallel programs (see T. Morishita et al. 2020 for a review). For example, the BoRG program (M. Trenti et al. 2011), which consisted of >1000 HST orbits collected through multiple HST Cycles, successfully identified $z \sim 8$–11 galaxy candidates at the bright-end magnitude range, $M_{\rm UV} \sim -21$ to -23 mag (L. D. Bradley et al. 2012; M. Trenti et al. 2012; K. B. Schmidt et al. 2014; S. R. Bernard et al. 2016; V. Calvi et al. 2016; T. Morishita et al. 2018, 2020). Identification of such luminous sources from a sufficiently large volume is critical to determine the shape of the luminosity function and its evolution with minimal cosmic variance (R. A. A. Bowler et al. 2014, 2020; R. J. Bouwens et al. 2015; R. C. Livermore et al. 2018; J. S. Bridge et al. 2019; K. Ren et al. 2019; S. Rojas-Ruiz et al. 2020; N. Leethochawalit et al. 2023a).

The unexpected detection of many luminous $z > 10$ galaxies with JWST demonstrates one reason that pure-parallel efforts are crucial to continue in the era of JWST. Pure-parallel imaging with NIRCam is ideally suited to robustly identify $z > 10$ galaxies and to characterize the shape of UV luminosity functions. Surveying many independent sightlines samples the Universe in an unbiased way and enables studies of galaxy evolution as a function of a wide range of environments (see also C. C. Williams et al. 2025, for their Cycle 1 NIRCam pure-parallel imaging program, PANORAMIC).

In addition, the pure-parallel mode is essentially at no cost in JWST primary observing time, thus enhancing current and planned programs in legacy fields. Thanks to the dichroic blue and red channels, pure-parallel imaging with NIRCam surveys is twice as efficient as on HST, and uniquely sample wavelengths of $>2\,\mu$m, which is inaccessible to wider-area optical—near-IR missions like Euclid and Roman.

Identified bright galaxies are ideal targets for follow-up spectroscopy from ground-based facilities (T. Treu et al. 2013; T. Morishita et al. 2020; G. Roberts-Borsani et al. 2022) and now with JWST. Early NIRSpec follow-up on previously identified HST BoRG sources confirmed 10 sources with <1 hr exposure times (G. Roberts-Borsani et al. 2024a; S. Rojas-Ruiz et al. 2024). However, the low-redshift contamination rate among these HST-selected sources was

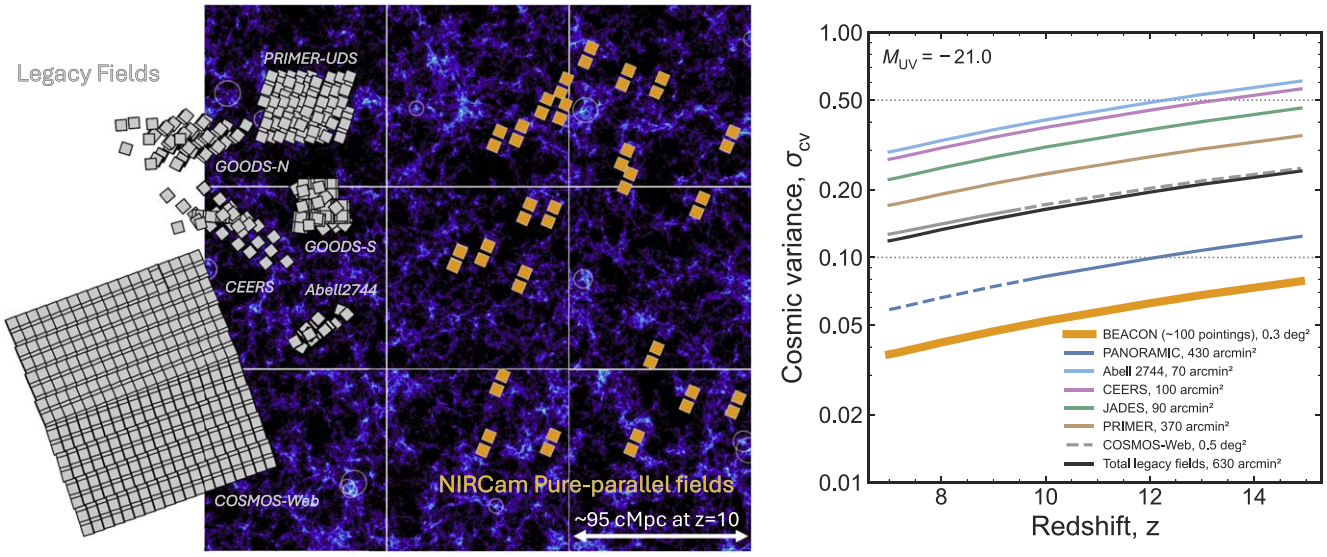

Figure 1. (Left): schematics of NIRCam pure-parallel imaging. Each pair of squares (orange) indicates the size of NIRCam imaging fields shown at a single arbitrary angle, overlaid on dark matter distribution at $z = 10$ from the THESAN simulation (R. Kannan et al. 2022; each of the nine panels has a size of ∼95 cMpc), where halos hosting massive galaxies ($>10^8\,M_\odot$) are encircled. For comparison, Cycle 1 and 2 surveys in legacy fields are shown (gray). (Right): cosmic variance, σ_{cv} in the UV luminosity function at $M_{UV} = -21$, as a function of the redshift for several JWST imaging programs (colored lines), compared to the expected cosmic variance in BEACON (thick orange line), and the total cosmic variance in legacy fields observed with at least eight NIRCam filters (A2744, JADES, CEERS, PRIMER), all estimated using the cosmic variance calculator by A. C. Trapp & S. R. Furlanetto (2020; see Section 2). Dashed lines indicate where contamination is expected to be high in surveys with fewer NIRCam filters.

significant—in the range of ∼20%−50% depending on the redshift, depth of observations, and available bands blueward of the Lyman break (N. Leethochawalit et al. 2023a). This was expected (e.g., B. Vulcani et al. 2017) and largely attributable to the small number of HST filters up to 1.6 μm (i.e., rest-frame $>$ 2000 Å at $z > 8$) and the lack of sensitive constraints at longer wavelengths that cover the rest-frame optical. Multiband JWST NIRCam imaging greatly improves our ability to obtain robust $z > 8$ galaxy samples with a much lower low-z interloper fraction (e.g., T. Morishita & M. Stiavelli 2023).

Here, we introduce Bias-free Extragalactic Analysis for Cosmic Origins with NIRCam (BEACON), a new JWST pure-parallel imaging survey approved for 600 pure-parallel hours in Cycle 2. BEACON is optimized to detect $z > 7.3$ Lyman-break galaxies, but also is capable of identifying lower redshift galaxies with up to eight-filter imaging. Surveying ∼100 high-latitude blank fields (equivalent to ∼0.3 deg^2) will allow for the identification of galaxies over a wide redshift range.

In this overview paper, we present the survey design and initial highlights from the first 19 observed fields. Dedicated studies of UV luminosity functions and galaxy properties will be presented in forthcoming papers (K. Kreilgaard 2025, in preparation; Y. Zhang 2025, in preparation). In Section 2, we outline the science goals of our program. We present the observing configurations and data reduction in Section 3, followed by a photometric analysis of the initial fields in Section 4. We release the initial data set on a dedicated webpage.[33]

Where relevant, we adopt the AB magnitude system (J. B. Oke & J. E. Gunn 1983; M. Fukugita et al. 1996), cosmological parameters of $\Omega_m = 0.3$, $\Omega_\Lambda = 0.7$, $H_0 = 70\,\mathrm{km\,s^{-1}\,Mpc^{-1}}$, and the G. Chabrier (2003) initial mass function.

[33] https://beacon-jwst.github.io

2. Survey Goals

BEACON takes advantage of the unique pure-parallel opportunity provided by the observatory to obtain 1−5 μm NIRCam imaging over ∼100 independent pointings. This enables a wealth of scientific investigations with minimal cosmic variance. We briefly describe our key science drivers.

2.1. Unbiased View of Galaxies in the First Billion Years

Early JWS observations discovered an unprecedented abundance of intrinsically luminous $z \gtrsim 10$ galaxy candidates (e.g., R. Bouwens et al. 2023; M. Castellano et al. 2022; C. T. Donnan et al. 2023; R. P. Naidu et al. 2022; C. M. Casey et al. 2024; Y. Harikane et al. 2024). Those luminous galaxies were not expected by theoretical models (e.g., P. Dayal et al. 2014; C. A. Mason et al. 2015; N. Mashian et al. 2016; P. Behroozi et al. 2019; S. Tacchella et al. 2018; L. Y. A. Yung et al. 2019; S. M. Wilkins et al. 2023), implying that some key physics is missing in the model of first galaxy formation. However, these detections have come from just ∼600 arcmin^2 of public imaging in legacy fields, and are subject to significant cosmic variance. In Figure 1, we show the fractional cosmic variance as a function of the redshift in JWST Cycle 1–2 programs, compared to the predicted cosmic variance in BEACON observations. We estimate the cosmic variance in the UV luminosity function (LF; $\sigma^2_{cv}(\phi) = [\langle\phi^2\rangle - \langle\phi\rangle^2]/\langle\phi\rangle^2$) at $M_{UV} = -21$, i.e., comparable to the UV magnitude of the brightest $z > 12$ galaxies confirmed by JWST: GHZ2/GLASS-z12 (M. Castellano et al. 2022; R. P. Naidu et al. 2022) and JADES-GS-z14-0 (S. Carniani et al. 2024), using the calculator by A. C. Trapp & S. R. Furlanetto (2020). We calculate the cosmic variance in multiple fields by summing the variance in quadrature following A. C. Trapp et al. (2023). Robustly measuring the bright end of the UV LF and its evolution at $z > 7$ requires *large* samples of $z > 7$ sources over a wide luminosity range and sufficient areas, to maximize statistical robustness against cosmic

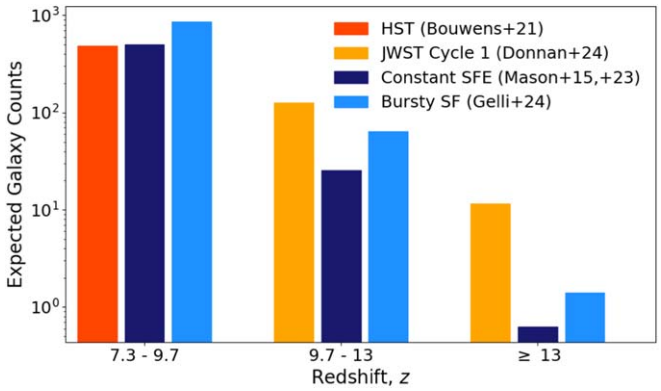

Figure 2. Expected numbers of sources in BEACON, shown for two theoretical models: constant star formation efficiency (dark blue; C. A. Mason et al. 2015, 2023) and bursty star formation (light blue; V. Gelli et al. 2024), and for two data-driven LFs: one determined from HST (red; R. J. Bouwens et al. 2021) and one from JWST Cycle 1 (orange; C. T. Donnan et al. 2024). All numbers are estimated assuming a flat 80% completeness down to the 10σ limiting magnitude. At $z \geqslant 13$ models predict hugely different number counts; thus BEACON will distinguish between scenarios.

variance. Crucially, Figure 1 shows how independent-sightline surveys such as BEACON and PANORAMIC efficiently reduce cosmic variance compared to contiguous fields. In particular, the A. C. Trapp & S. R. Furlanetto (2020) model predicts that BEACON will reach ∼5% cosmic variance in the bright end of the UV LF at $z \sim 12$, compared to ∼20% cosmic variance in both a large contiguous area with COSMOS-Web, which covers a ∼70% larger area with a smaller filter set (four NIRCam filters), and to the combination of deep JWST surveys in legacy fields (A2744, CEERS, JADES, and PRIMER).

In Figure 2, we show the expected number of galaxies that BEACON will find, assuming that the survey will reach 80% completeness down to 10σ limiting magnitudes. For the allocated 600 hr (see also Section 3), we expect to find 500–1000 galaxies at $z \geqslant 7.3$ and 25–125 galaxies in the redshift range $9.7 \leqslant z \leqslant 13$, depending on the model used. The most interesting redshift range is $z \geqslant 13$, where the predicted numbers from different models deviate the most. For example, a model assuming redshift-independent star formation efficiency even with no dust obscuration (C. A. Mason et al. 2015, 2023), predicts just one galaxy, whereas the LF based on early Cycle 1 fields (C. T. Donnan et al. 2024) predicts 12 galaxies and a bursty star formation model (V. Gelli et al. 2024) predicts a few. By the completion of our survey, we will have an improved census of galaxies in the first billion years.

2.2. Cosmic Noon—Build-up of Stellar Mass and Structures

Galaxies at $z \sim 2$ appear significantly different from those in the local Universe—with clumpy and disturbed features from star formation (e.g., B. G. Elmegreen & D. M. Elmegreen 2005; N. M. Förster Schreiber et al. 2009; R. Genzel et al. 2011; K. Guo et al. 2015), or compact morphology for post-starburst and passively evolving galaxies (e.g., E. Daddi et al. 2005; I. Damjanov et al. 2009; G. Barro et al. 2017; D. J. Setton et al. 2022). The discovery of already quenched populations at $z > 3$ (e.g., K. Glazebrook et al. 2017; C. Schreiber et al. 2018; M. Tanaka et al. 2019; F. Valentino et al. 2020), some of which are clustered (K. Ito et al. 2024; M. Tanaka et al. 2024), suggests a very early and rapid build-up of stellar mass. Early JWST NIRCam studies identified several massive galaxies at $z \sim 4$–7 (A. C. Carnall et al. 2023, 2023; K. Glazebrook et al. 2024; A. Weibel et al. 2024). The prevalence of many evolved galaxies in such an early epoch would invoke a critical, but intriguing, need for updates to the current galaxy evolution and quenching models (e.g., M. Boylan-Kolchin 2023; C. C. Lovell et al. 2023). Further identification requires a larger volume to build a complete picture of massive galaxy build-up.

BEACON will enable the search for massive galaxies at $2 < z < 7$, over a total volume of $\sim 10^7$ Mpc^3. Based on our magnitude limits and the mass functions from I. Davidzon et al. (2017) and J. R. Weaver et al. (2023), we expect that $\sim 10^5$ galaxies of $M_* > 10^9\,M_\odot$ will be identified, including several $\log M^*/M_\odot > 3 \times 10^{10}\,M_\odot$ galaxies at $z > 5$. The star formation activity of these galaxies will be characterized by, e.g., the rest-frame *UVJ* diagram (R. J. Williams et al. 2009; F. Valentino et al. 2023). The wavelength coverage from contiguous filters out to ∼5 μm will secure galaxy samples of currently missed quiescent and dust-enshrouded optical-dark galaxy populations (L. Barrufet et al. 2025; T. Wang et al. 2024), allowing for a comprehensive study of their properties, including their dependence on local environments, characterized by an overdensity factor $\delta = (n - \bar{n})/\bar{n}$ (T. Morishita et al. 2025a, 2025b) or phot-z weighted two-dimensional kernel density analysis (e.g., N. Chartab et al. 2020; M. Brinch et al. 2023). Furthermore, HST pure-parallels demonstrated statistics measured in many uncorrelated fields and provided novel measurements of galaxy/dark matter halo bias (A. J. Cameron et al. 2019). The superb photometric quality will enable searches for candidate overdensities of galaxies (e.g., A. B. Newman et al. 2014).

2.3. Nearby Universe—Dwarfs and Galaxies

Early Release Science and Cycle 1 programs clearly showed that a few hours of exposure time with JWST are comparable to the deepest fields observed by HST. BEACON will provide a unique and extensive data set for legacy science, including enabling follow-up spectroscopy of exciting targets in future JWST cycles. Some legacy science highlights are:

(1) Study of brown dwarfs in the Milky Way, to probe its structure from random sightline observations (R. E. Ryan et al. 2011; B. W. Holwerda et al. 2014, 2018). The wavelength coverage at >1.6 μm is critical to characterize (sub)dwarf populations (A. C. Schneider et al. 2020; M. Nonino et al. 2023; A. J. Burgasser et al. 2024; K. N. Hainline et al. 2024).

(2) Dust properties of galaxies at $z \sim 0$: Stellar continuum and dust emission coexist in the rest frame 1–5 μm. NIRCam filters will enable starburst/AGN diagnostics with the F200W − F444W color (e.g., B. Vulcani et al. 2023) and 3.3 μm polycyclic aromatic hydrocarbon (PAH) features measured with F356W flux excess (e.g., H. Inami et al. 2018) for those with accurate redshift measurements.

3. Survey Design

3.1. Pure-parallel Observations with JWST

JWST offers a pure-parallel observing mode,[34] in which one instrument is used while another serves as the primary. This is similar to the pure parallel mode operated by HST (H. Atek et al. 2011; M. Trenti et al. 2011; H. Yan et al. 2011). With JWST, pure-parallel observations can utilize a variety of

[34] https://jwst-docs.stsci.edu/jppom/parallel-observations

instruments (i.e., NIRCam, NIRISS, and MIRI as of Cycle 2). The pure-parallel use of NIRCam is analogous to the HST's use of WFC3-IR, as seen in the BoRG survey (M. Trenti et al. 2011). However, there are significant differences with NIRCam's pure-parallel imaging: (1) extended red wavelength coverage (5 μm versus 1.7 μm), (2) a larger effective field of view (FoV) per image (9.7 arcmin^2 versus 4.6 arcmin^2), and (3) dichroic imaging capability, allowing for simultaneous short- and long-wavelength observations. The combination of the second and third points makes JWST's NIRCam pure-parallel mode approximately four times more efficient than HST's, even before considering the significant sensitivity differences (i.e., $m_{\rm H} = 28.4$ mag versus 26.6 mag at 10σ, 1 hr exposure). Additionally, JWST's primary observing modes are typically equipped with dithering, which benefits parallel imaging by reducing potential contamination from detector artifacts and cosmic rays, whereas this has not been often the case for HST's pure-parallel observations.

JWST's pure-parallel mode, however, introduces high complexity, resulting in stringent requirements for scheduling and filter configurations. JWST does not allow for mechanical movement during the primary dither, resulting in less flexibility when distributing exposure time across multiple filters in a given pointing. In particular, JWST can offer a very long exposure per visit, whereas HST is limited to a maximum exposure of $\sim$2800 s due to the interruption from its orbit occultation. This in general helps the primary observations reduce the overhead, but it also means *fewer opportunities* for the parallel to reconfigure optical elements. Additionally, the complexity of the spectroscopic observing modes necessitates careful consideration of data rates over the number of independent exposures.

Among the allocated opportunities, we prioritized those that offer four or more "group slots" (corresponding to the number of short/long-filter pairs) within the same field. As pure-parallel availability is determined by the setup of primary programs on the schedule, not all the allocated opportunities have at least four slots. Thus, we also utilize observations with fewer slots when they either (i) provide sufficient depth, $>$1000 s ($\sim$20% of executed/scheduled visits have $\leqslant$2 slots) or (ii) include existing NIRCam data covering most of the FoV from previous observations ($\sim$10%), which can be combined with the new data. We discuss the selection of filters in more detail in Section 3.3.

3.2. Exposure Configuration

Each exposure is set to optimize the signal-to-noise ratio (SNR) and meet the data volume limitation. The total data volume is significantly affected by the configuration of each primary observation. As such, careful consideration for each visit on the Astronomer's Proposal Tool is required. Our default is to use the SHALLOW4 readout mode, which allows for reasonable exposure and SNR without suffering from saturation. When data volume is severely limited, we use a longer readout mode, i.e., DEEP8 or DEEP2, which are more subject to saturation for bright sources.

3.3. Filter Configuration

Taking advantage of NIRCam dichroic, our default filter configuration consists of eight filters ($0.8 < \lambda/\mu{\rm m} < 5.0$), pairing the four long-wavelength filters (F277W, F356W, F410M, F444W) with four short-wavelength ones (F090W, F115W, F150W, F200W; Figure 3). This means that we require a minimum of four group slots in the primary program, where each group slot consists of an entire dither sequence. However, due to the limited availability of parallel slots, our program utilizes opportunities of less than four group slots (see below).

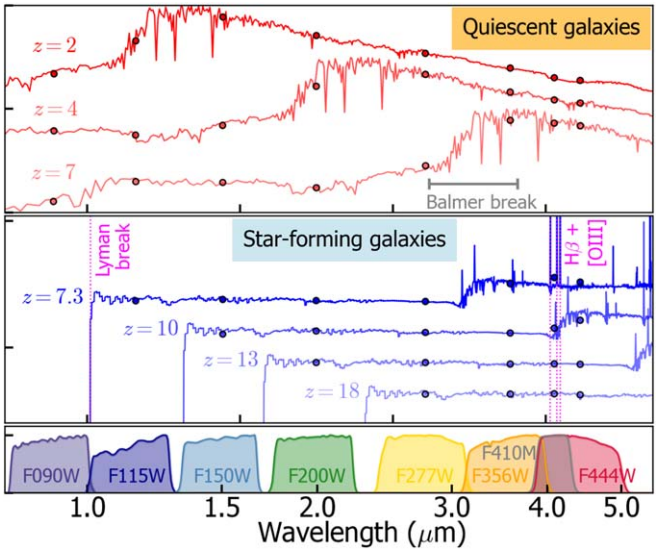

Figure 3. Template SEDs of galaxies at various redshifts, along with the transmission curves of our default filter set.

Those eight NIRCam filters securely capture the Lyman break of galaxies at $z > 7$ and the Balmer break for galaxies at $2 < z < 7$. The almost uninterrupted, nonoverlapping filter choice at 0.8–5 μm allows us a complete sampling of galaxies at these redshift ranges. In addition to the Lyman break, the Balmer break sampled by F277W/F356W/F410M/F444W is critical to characterize stellar populations of galaxies at $z \lesssim 10.5$ (e.g., H. Katz et al. 2024; C. Witten et al. 2025), as well as to capture extreme line emission from Hβ+[O III] at $7 < z < 9$ by measuring flux excess in F410M/F444W (e.g., R. Endsley et al. 2023; M. Llerena et al. 2024). While each visit is largely subject to the primary observation, we distribute the allocated time among filters by optimizing for our high-z dropout selection. Namely, we allocate the deepest slots to the bluest filter (F090W) to secure the dropout at $z > 7$, and the medium-band filter F410M to compensate for its relatively lower sensitivity. When five or more group slots are available, we include other medium-band filters (F140M, F182M, F210M, F430M, F460M), which increase the redshift reliability and expand the redshift range of strong-line emitter searches.

For parallel opportunities where only three group slots are available, we configure those with F090W, F115W, F150W, F277W, F356W, and F444W. This strategy keeps a redshift range similar to that for the full filter case. We utilize opportunities with fewer filters only when there are available data in the overlapping area; for those, we select unused filters to increase wavelength sampling.

We note that several visits so far were skipped in our executed observations, due to scheduling issues (unexpected changes in the primary observations) or data transfer limits during the visits. Consequently, those affected fields may have

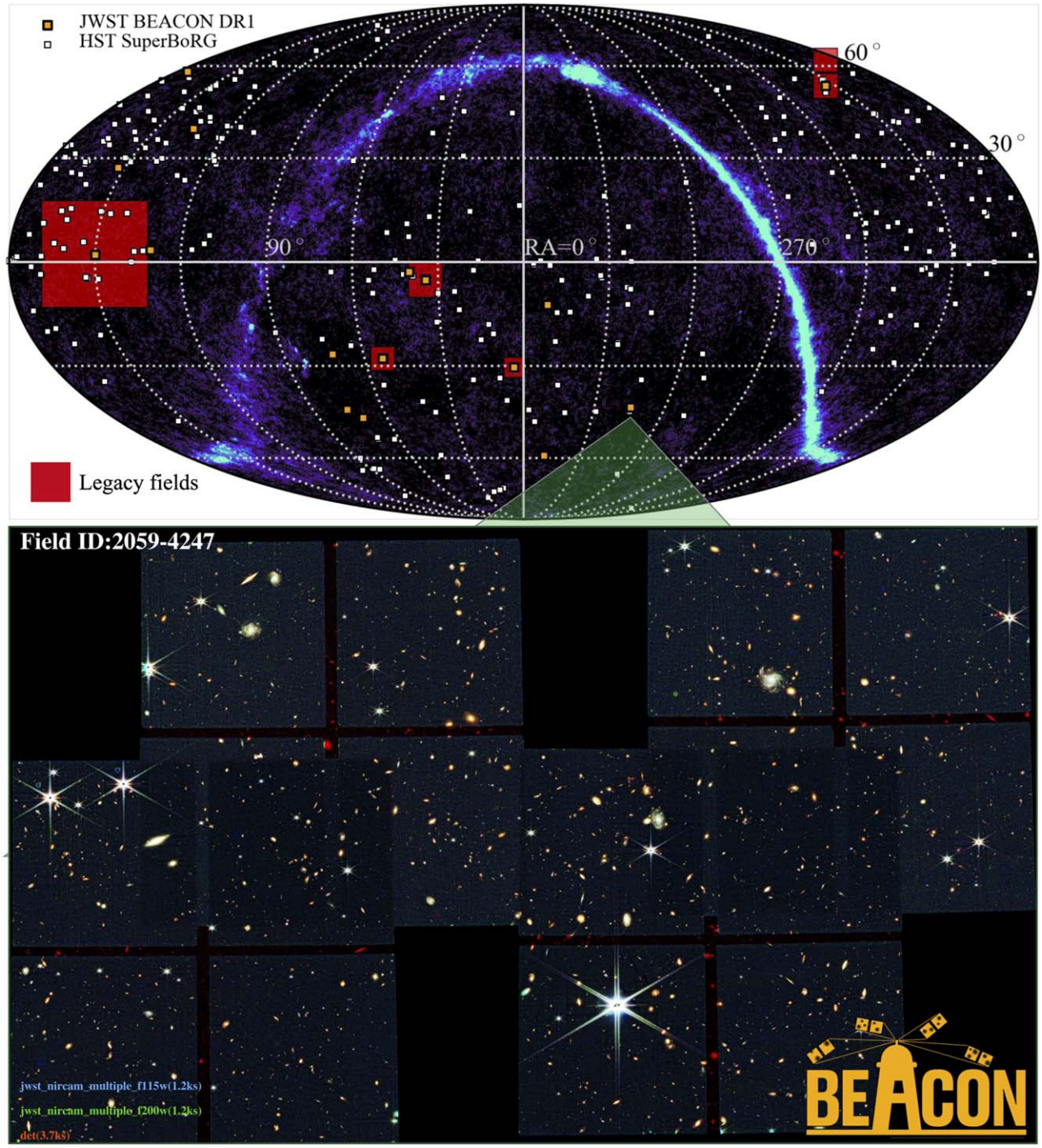

Figure 4. (Top): sky distributions of the 19 BEACON DR1 fields (orange squares), overlaid on a temperature map from the WMAP 7 yr data (N. Jarosik et al. 2011). Also shown are legacy fields of JWST (COSMOS-Web, PRIMER-UDS, CEERS-EGS, JADES-GOODS-South, JADES-GOODS-North, and A2744; red squares) and the HST's pure-parallel imaging fields from HST SuperBoRG (white squares; $N = 316$). The symbol sizes are not the actual sky size but are roughly scaled to the corresponding survey area. (Bottom): RGB color composite image of one of the DR1 fields.

shorter total exposures than planned, or only partial filter coverage, or in some cases no observations.

4. Data Analysis Overview

4.1. Imaging Data Reduction

In this study, we reduce and analyze data taken in the first 19 fields. The sky distributions of the fields are shown in Figure 4. We follow an approach similar to that presented by T. Morishita & M. Stiavelli (2023) for the reduction of images. Briefly, our pipeline retrieves the raw-level images from the Mikulski Archive for Space Telescopes archive when they become available after each observation, and then reduces them with the official JWST pipeline. Our pipeline adds several custom steps including $1/f$-noise subtraction using `bbpn`,[35] snowball masking using `Grizli` (G. Brammer et al. 2022),

[35] https://github.com/mtakahiro/bbpn

and additional cosmic-ray masking using `lacosmic` (P. G. van Dokkum 2001; L. Bradley 2023). The final drizzled images, with the pixel scale set to $0\farcs0315\,\mathrm{pixel}^{-1}$, are aligned to the IR-detection image, i.e., a coadded image of F277W+F356W+F444W filters weighted by inverse variance maps. The filter choice was made to secure the detection of both high-z galaxies and red (dusty or quiescent) galaxies.

To homogenize the point-spread function (PSF) of the NIRCam images with that of F444W, we generate convolution kernels using PSFs generated with `webbpsf`.[36] We provide those PSFs to `pypher` (A. Boucaud et al. 2016) and generate convolution kernels for each filter. The quality of convolved PSFs is within $\ll$1% agreement in the encircled flux at radius $r = 0\farcs16$, i.e., the size used for our photometric flux measurements.

4.2. Photometry

We identify sources in the detection image using `Source Extractor` (E. Bertin & S. Arnouts 1996). We measure source fluxes on PSF-matched mosaic images with a fixed aperture of radius $0\farcs16$. We set the configuration parameters of the `Source Extractor` as follows: DETECT_MINAREA 0.0081 arcsec^2, DETECT_THRESH 1.0, DEBLEND_NTHRESH 64, DEBLEND_MINCONT 0.0001, BACK_SIZE 128, and BACK_FILTSIZE 5.

The aperture-based fluxes measured for each source are then scaled by a single factor, defined as $f_{\mathrm{auto,F444W}}/f_{\mathrm{aper,F444W}}$, to the total flux, where f_{auto} is the flux measured within elliptical Kron apertures with the 2.5 scaling factor. With this approach, colors remain as those measured in the aperture, whereas the fluxes used in the following analyses (for the derivation of stellar mass and star formation rate) are scaled up to the total quantities.

It is known that the photometric flux error of space-based images is often underestimated, partially due to the correlation between pixels introduced by the pipeline's `drizzling` step (e.g., S. Casertano et al. 2000). The rms maps generated by the pipeline thus need to be scaled so that it represents more realistic flux uncertainties. To estimate the scaling factor, we follow the method presented in M. Trenti et al. (2011). Briefly, we place 300 apertures in randomly selected empty regions of each image and measure the fluxes therein in the same way for real sources. The rms map is multiplied by a scale factor so that the standard deviation of the fluxes in those empty apertures and the median of the flux errors returned by SExtractor would match.

Once the fluxes and errors are measured and scaled, Galactic dust reddening is corrected using the attenuation value retrieved for the coordinates of each field from the NASA/IPAC Extragalactic Database (D. J. Schlegel et al. 1998; E. F. Schlafly & D. P. Finkbeiner 2011). We adopt the canonical Milky Way dust law for the reddening curve (J. A. Cardelli et al. 1989).

The average limiting magnitudes of the images are measured in regions where no source is detected among the effective area (i.e., sky area), using apertures of $0\farcs16$ radius, and reported in Table 1. The average limiting magnitude of the DR1 fields and the total area are shown in Figure 5, together with those of the aforementioned JWST surveys and several HST surveys (N. A. Grogin et al. 2011; A. M. Koekemoer et al. 2011; R. S. Ellis et al. 2013; G. D. Illingworth et al. 2013; R. J. Bouwens et al. 2019).

[36] https://github.com/spacetelescope/webbpsf

4.3. Photometric Redshift

For each field, we produce a photometric catalog by running `eazy` (G. B. Brammer et al. 2008). Our default setup is similar to what was presented in T. Morishita et al. (2023), using a template library provided by K. N. Hainline et al. (2024). This template library supplements `eazy`'s default library (v1.3) by adding young, line-emitting galaxy templates generated with `fsps` (C. Conroy et al. 2009). The increased variety of fitting templates thus enables a more comprehensive redshift estimate for target young galaxies. The redshift range of fitting is set to $0 < z < 30$, with a step size of $0.01(1+z)$. We adopt a default magnitude prior provided by `eazy`, using one of the three NIRCam red channel broad filters (F277W, F356W, F444W) based on their availability in each field.

We utilize the output likelihood function derived by `eazy` to estimate a statistical redshift range for each source. We adopt the median redshift calculated using the full $p(z)$ distribution as the best-fit redshift and estimate 1σ uncertainties by taking the differences from the 16th and 84th percentile redshifts. The redshift measurements and the probability distributions are used in our high-z galaxy selection (Section 5.2). Absolute UV magnitudes (M_{UV}) are calculated using the best-fit template at the corresponding redshifts.

4.4. Photometric Selection of High-redshift Galaxies

We identify candidate galaxies at $z > 7$ via the Lyman-break dropout method (C. C. Steidel et al. 1998). Following a similar approach presented in T. Morishita & M. Stiavelli (2023), and T. Morishita et al. (2024), we first apply the following color selection:

F090W dropouts ($7.3 \lesssim z \lesssim 9.7$)
$$\mathrm{S/N}_{150} > 4$$
$$\mathrm{S/N}_{090} < 2$$
$$z_{\mathrm{set}} = 6,$$

F115W dropouts ($9.7 \lesssim z \lesssim 13$)
$$\mathrm{S/N}_{200} > 4$$
$$\mathrm{S/N}_{115,090} < 2$$
$$z_{\mathrm{set}} = 8,$$

F150W dropouts ($13 \lesssim z \lesssim 18$)
$$\mathrm{S/N}_{277} > 4$$
$$\mathrm{S/N}_{150,115,090} < 2$$
$$z_{\mathrm{set}} = 10,$$

where available filters that are bluer than the rest-frame wavelength of <1216 Å are used for 2σ nondetection. Furthermore, to secure nondetection, we repeat the nondetection step with a smaller aperture, $r = 0\farcs08$ ($\sim$2.5 pixels). Note that a photometric selection is not attempted for redshift windows where no dropout filter is available. z_{set} is a redshift limit used to calculate total low-z probabilities (see below).

After securing nondetection in blue filters, we apply a photometric redshift selection. Following T. Morishita et al. (2018), in each dropout selection we exclude sources that do not satisfy $p(z > z_{\mathrm{set}}) > 0.8$, i.e., total redshift probability at $z > z_{\mathrm{set}}$ is less than 80%, where z_{set} is defined above separately for each selection redshift window. The combination of the detection/nondetection requirement and the phot-z analysis

Table 1
5σ Limiting Magnitudes for Point Sources Are Shown

FLDID	R.A. (deg.)	Decl. (deg.)	F090W		F115W		F150W		F200W		F277W		F356W		F410M		F444W	
			$t_{\rm exp}$	$m_{5\sigma}$	$t_{\rm exp}$	$m_{5\sigma}$	$t_{\rm exp}$	$m_{5\sigma}$	$t_{\rm exp}$	$m_{5\sigma}$	$t_{\rm exp}$	$m_{5\sigma}$	$t_{\rm exp}$	$m_{5\sigma}$	$t_{\rm exp}$	$m_{5\sigma}$	$t_{\rm exp}$	$m_{5\sigma}$
0014−3025	3.59520	−30.41974	10.0	28.9	10.0	28.8	⋯	⋯	10.0	29.1	10.0	29.1	10.0	29.3	⋯	⋯	10.0	29.0
0217−0509	34.21885	−5.13408	18.9	29.3	13.1	29.0	13.1	29.2	⋯	⋯	13.1	29.1	13.1	29.2	⋯	⋯	18.9	28.8
0217−0508	34.29253	−5.12272	18.9	29.4	13.1	29.0	13.1	29.2	⋯	⋯	13.1	29.2	13.1	29.2	⋯	⋯	18.9	28.9
0217−0504	34.30829	−5.07792	18.9	29.2	13.1	29.0	13.1	29.2	⋯	⋯	13.1	29.5	13.1	29.6	⋯	⋯	18.9	29.3
0240−0253	40.09595	−2.87019	1.0	26.9	1.0	26.9	1.0	27.2	⋯	⋯	1.0	28.0	1.0	28.1	⋯	⋯	1.0	27.5
0332−2749	53.03300	−27.81392	16.1	29.4	16.1	29.4	1.2	28.0	16.1	29.7	16.1	29.4	1.2	28.5	16.1	29.1	16.1	29.3
0332−2745	53.03766	−27.75151	7.5	28.9	7.5	29.0	7.5	29.1	12.5	29.3	7.5	29.6	7.5	29.5	⋯	⋯	20.0	29.2
0442−4613	70.42773	−46.21713	0.7	26.6	0.5	26.1	0.5	26.4	⋯	⋯	0.5	27.5	0.5	27.5	⋯	⋯	0.7	27.7
0447−2637	71.67559	−26.60116	1.2	27.6	1.2	27.4	1.2	27.9	1.2	28.1	1.2	28.6	1.2	28.5	1.2	27.9	1.2	28.2
0502−4338	75.45100	−43.63230	⋯	⋯	1.0	27.5	1.0	27.8	1.0	28.0	1.0	28.5	1.0	28.5	⋯	⋯	1.0	28.2
0843+0324	130.65348	3.41877	⋯	⋯	0.8	27.6	0.8	27.8	0.8	27.9	0.8	28.3	0.8	28.3	⋯	⋯	0.8	27.8
0860+3857	134.98519	38.96236	2.5	27.9	1.6	27.5	1.6	27.7	⋯	⋯	1.6	28.5	1.6	28.5	⋯	⋯	2.5	28.2
0959+0200	149.84149	2.01664	3.3	28.3	3.3	28.3	3.3	28.5	3.3	28.6	3.3	28.9	3.3	28.9	3.3	28.2	3.3	28.5
1010+2701	152.44541	27.03744	4.2	28.1	4.2	28.1	4.2	28.4	⋯	⋯	4.2	28.7	4.2	28.7	⋯	⋯	4.2	28.3
1138+5748	174.41601	57.80085	1.4	27.4	1.4	27.3	1.4	27.6	⋯	⋯	1.4	28.5	1.4	28.4	⋯	⋯	1.4	28.1
1420+5252	215.07468	52.86999	3.4	28.0	3.4	28.1	3.4	28.3	3.4	28.5	3.4	28.9	3.4	28.9	3.4	28.2	3.4	28.6
2059−4247	314.63703	−42.78990	⋯	⋯	1.2	27.0	1.2	27.3	1.2	27.4	1.2	28.0	1.2	28.1	⋯	⋯	1.2	27.6
2316−5910	349.11637	−59.15965	⋯	⋯	1.8	27.0	1.8	27.3	1.8	27.5	1.8	28.1	1.8	28.2	⋯	⋯	1.8	27.8
2325−1216	351.35492	−12.26333	⋯	⋯	1.0	26.5	1.0	26.8	1.0	26.8	1.0	27.7	1.0	27.8	⋯	⋯	1.0	27.6

Note. Exposure times are shown in units of 1000 s.

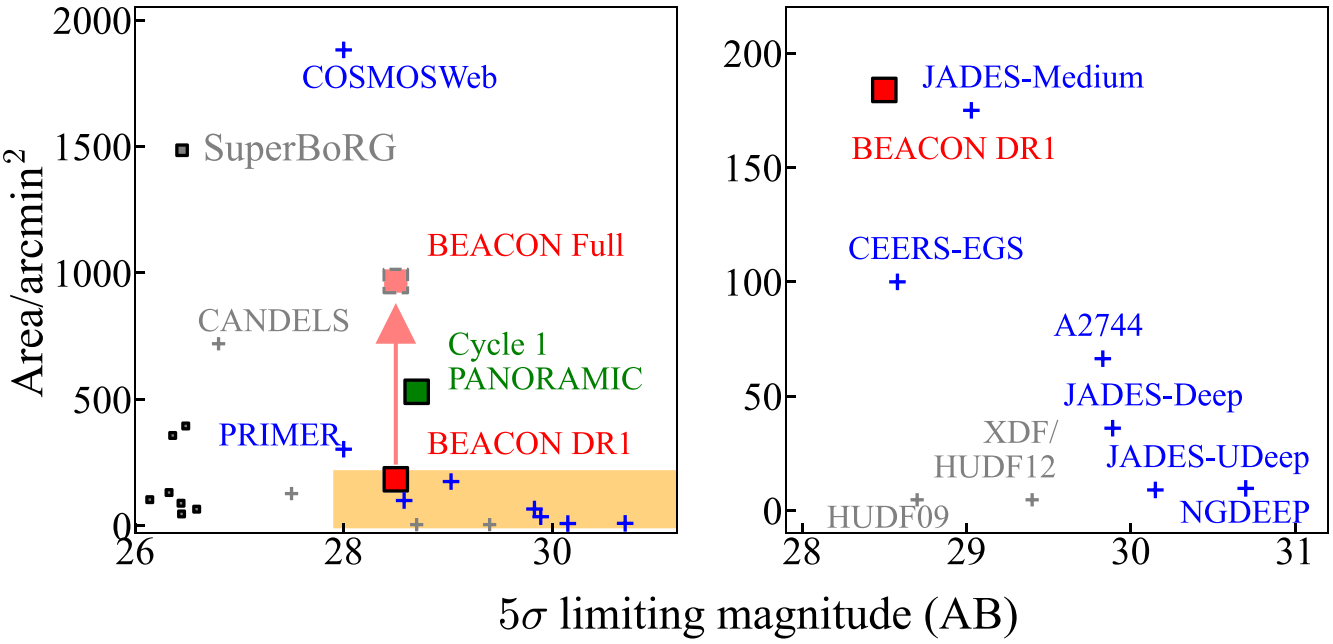

Figure 5. Limiting magnitudes and survey areas of BEACON and various JWST programs (symbols in color); COSMOS-Web (C. M. Casey et al. 2023), PRIMER (C. T. Donnan et al. 2024), PANORAMIC (C. C. Williams et al. 2025), JADES (D. J. Eisenstein et al. 2023), CEERS (S. L. Finkelstein et al. 2023), A2744 (R. Bezanson et al. 2024; T. Treu et al. 2022), NGDEEP (M. B. Bagley et al. 2023b). Square and cross symbols represent pure-parallel and legacy surveys, respectively. Several HST programs are also shown in gray (see T. Morishita 2021 for the full description). The region hatched in orange is shown in zoom in the right panel.

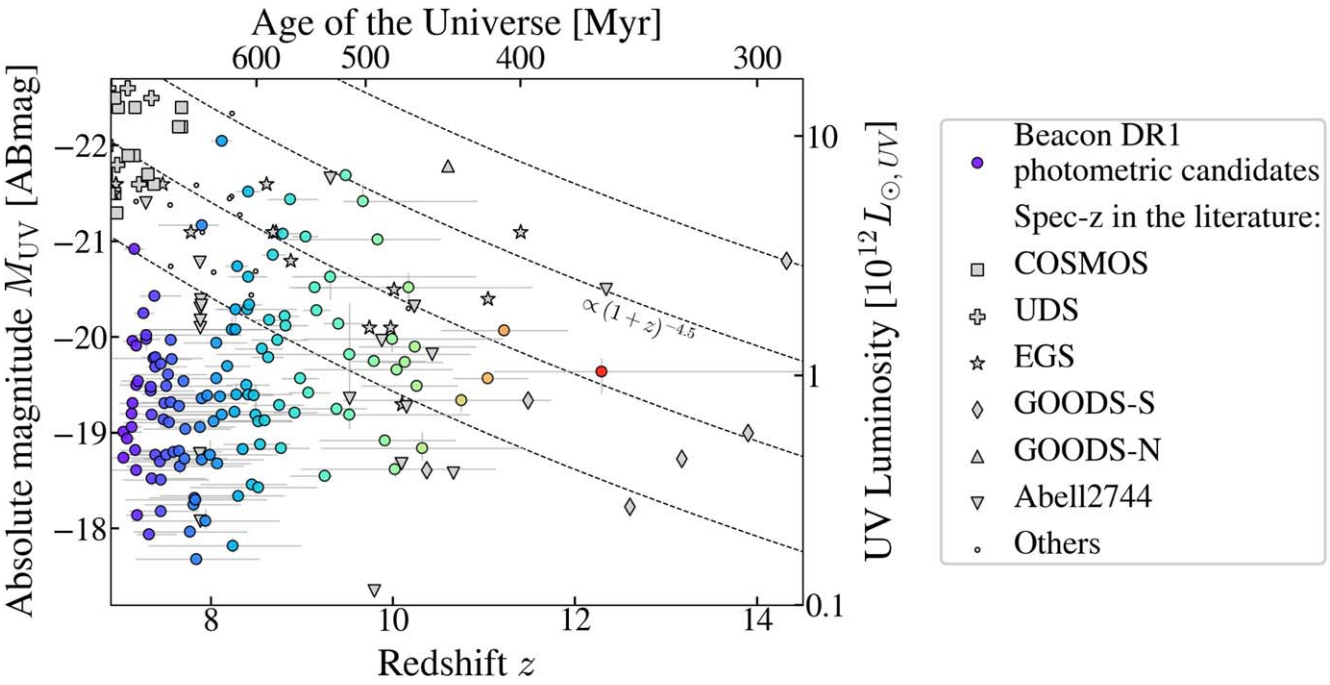

Figure 6. Redshift–M_{UV} distributions of final photometric candidates selected from the 19 DR1 fields (circles, colored by redshift). Semiempirical luminosity evolution curves, $\propto (1+z)^{-4.5}$, of halos of a given comoving abundance are shown (dashed lines). Spectroscopically confirmed sources in the literature are shown (gray symbols; P. Arrabal Haro et al. 2023; E. Curtis-Lake et al. 2023; Y. Harikane et al. 2023c; T. Morishita et al. 2023; S. Carniani et al. 2024; M. Castellano et al. 2024; L. Napolitano et al. 2025; G. Roberts-Borsani et al. 2024b).

provides us with sources whose phot-z solution is consistent with the dedicated redshift range of each dropout selection.

We have tested R. L. Larson et al. (2023b)'s templates and found that the results are overall unchanged. A detailed comparison among several template sets and various SED fitting software will be presented in a forthcoming paper (Y. Zhang et al., in preparation).

5. Initial Results

5.1. Overview of the Observed Fields

In this overview paper, we focus on the first 19 fields taken (hereafter Data Release 1, or DR1, fields). Results from the full fields will be presented upon completion of the program in forthcoming papers. In Table 1, we summarize the DR1 fields.

Table 2
Selected High-z Galaxy Candidates

ID	R.A.	Decl.	$m_{\rm F150W}$	$m_{\rm F444W}$	z	$M_{\rm UV}$
beacon_0217-0509-1447	34.225235	−5.182756	28.1	27.5	$7.04^{+0.20}_{-0.18}$	$-19.01^{+0.01}_{-0.02}$
beacon_0217-0508-9736	34.293415	−5.115285	28.4	28.7	$7.04^{+0.37}_{-0.18}$	$-18.74^{+0.01}_{-0.01}$
beacon_1420+5252-7386	215.037430	52.877472	28.2	27.4	$7.08^{+0.09}_{-0.08}$	$-18.94^{+0.01}_{-0.01}$
beacon_1420+5252-12023	215.039520	52.891056	28.1	27.8	$7.13^{+0.11}_{-0.13}$	$-19.06^{+0.01}_{-0.01}$
beacon_1420+5252-7298	215.038239	52.877132	27.7	27.4	$7.13^{+0.11}_{-0.13}$	$-19.20^{+0.01}_{-0.01}$
beacon_1420+5252-9579	215.037079	52.892605	27.2	26.7	$7.14^{+0.10}_{-0.11}$	$-19.96^{+0.01}_{-0.01}$
beacon_1420+5252-3062	215.040863	52.863846	27.8	27.5	$7.14^{+0.12}_{-0.15}$	$-19.31^{+0.01}_{-0.01}$
beacon_1420+5252-10296	215.125000	52.874062	26.2	25.8	$7.16^{+0.11}_{-0.12}$	$-20.92^{+0.01}_{-0.01}$
beacon_0217-0504-6307	34.273205	−5.037470	28.2	27.1	$7.17^{+0.19}_{-0.17}$	$-18.82^{+0.02}_{-0.02}$
beacon_0217-0509-4631	34.241405	−5.150918	28.6	28.6	$7.18^{+0.45}_{-0.36}$	$-18.61^{+0.05}_{-0.06}$
beacon_0959+0200-14013	149.833344	2.036179	27.5	27.4	$7.18^{+0.23}_{-0.18}$	$-19.50^{+0.01}_{-0.01}$
beacon_1420+5252-12575	215.025375	52.891273	27.2	26.1	$7.18^{+0.05}_{-0.07}$	$-19.91^{+0.01}_{-0.01}$
beacon_0217-0504-2657	34.272232	−5.045108	28.9	27.6	$7.19^{+0.24}_{-0.12}$	$-18.14^{+0.01}_{-0.01}$
beacon_1420+5252-1569	214.994904	52.866634	27.6	27.3	$7.20^{+0.11}_{-0.19}$	$-19.54^{+0.01}_{-0.01}$
beacon_1138+5748-6058	174.370514	57.791782	26.8	26.0	$7.26^{+0.11}_{-0.11}$	$-20.25^{+0.01}_{-0.01}$
beacon_0959+0200-92	149.819672	1.965411	27.2	26.8	$7.29^{+0.16}_{-0.18}$	$-19.98^{+0.01}_{-0.01}$
beacon_0860+3857-14167	134.982468	38.985676	27.0	26.1	$7.29^{+1.05}_{-0.13}$	$-20.02^{+0.16}_{-0.01}$
beacon_0217-0508-8517	34.283566	−5.124747	29.1	29.0	$7.32^{+0.30}_{-0.13}$	$-17.94^{+0.01}_{-0.01}$
beacon_0332-2745-7700	53.071823	−27.782648	27.8	27.4	$7.34^{+0.49}_{-0.15}$	$-19.44^{+0.04}_{-0.01}$
beacon_0959+0200-1159	149.840607	1.964149	27.9	27.3	$7.34^{+0.14}_{-0.17}$	$-19.48^{+0.01}_{-0.01}$
beacon_0014-3025-10125	3.625879	−30.439075	…	27.9	$7.35^{+0.60}_{-0.07}$	$-18.52^{+0.08}_{-0.01}$
beacon_0332-2745-8900	53.053425	−27.765003	27.8	26.8	$7.35^{+0.08}_{-0.10}$	$-19.19^{+0.01}_{-0.01}$
beacon_1138+5748-3075	174.362335	57.780087	27.3	26.9	$7.37^{+0.54}_{-0.47}$	$-19.78^{+0.08}_{-0.06}$
beacon_1010+2701-3159	152.407913	27.005966	26.9	26.9	$7.38^{+0.29}_{-0.16}$	$-20.43^{+0.01}_{-0.01}$
beacon_0332-2745-15094	53.046597	−27.738073	27.3	27.5	$7.39^{+0.20}_{-0.15}$	$-19.79^{+0.01}_{-0.01}$
beacon_0332-2749-5025	53.086330	−27.823927	27.4	26.6	$7.39^{+0.35}_{-0.10}$	$-19.69^{+0.01}_{-0.01}$
beacon_0959+0200-1349	149.829239	1.969253	28.2	28.5	$7.39^{+0.43}_{-0.38}$	$-18.77^{+0.03}_{-0.04}$
beacon_0332-2745-13954	53.086193	−27.773207	28.6	28.4	$7.44^{+0.42}_{-0.36}$	$-18.70^{+0.04}_{-0.04}$
beacon_0217-0504-17278	34.329090	−5.092696	28.7	28.5	$7.45^{+0.53}_{-0.42}$	$-18.51^{+0.05}_{-0.06}$
beacon_0217-0504-6678	34.284660	−5.053731	29.0	29.0	$7.45^{+0.42}_{-0.35}$	$-18.18^{+0.04}_{-0.03}$
beacon_1420+5252-3630	215.084747	52.858551	27.7	27.6	$7.45^{+0.07}_{-0.08}$	$-19.72^{+0.01}_{-0.01}$
beacon_0217-0508-1040	34.320229	−5.164967	28.1	28.7	$7.48^{+0.45}_{-0.36}$	$-19.14^{+0.03}_{-0.04}$
beacon_0217-0504-10666	34.311810	−5.084851	28.0	26.8	$7.49^{+0.92}_{-0.23}$	$-19.31^{+0.08}_{-0.03}$
beacon_1420+5252-11406	215.110046	52.872971	28.5	28.6	$7.51^{+0.55}_{-0.47}$	$-18.77^{+0.05}_{-0.04}$
beacon_0217-0504-18177	34.323090	−5.081106	27.7	26.9	$7.51^{+0.73}_{-0.35}$	$-19.49^{+0.07}_{-0.04}$
beacon_0959+0200-13202	149.845184	2.029492	27.6	27.4	$7.53^{+0.43}_{-0.42}$	$-19.61^{+0.05}_{-0.04}$
beacon_0332-2745-10227	53.062523	−27.768053	28.2	27.5	$7.54^{+0.38}_{-0.50}$	$-19.11^{+0.05}_{-0.07}$
beacon_0332-2745-8698	53.053013	−27.765186	27.9	27.7	$7.56^{+0.48}_{-0.33}$	$-19.32^{+0.03}_{-0.03}$
beacon_0447-2637-2129	71.703773	−26.632273	27.1	26.5	$7.56^{+0.08}_{-0.07}$	$-19.97^{+0.01}_{-0.01}$
beacon_0217-0509-1974	34.221172	−5.180426	27.4	27.8	$7.57^{+0.22}_{-0.22}$	$-19.77^{+0.01}_{-0.01}$
beacon_0217-0509-6250	34.214062	−5.142040	28.4	28.2	$7.59^{+0.53}_{-0.46}$	$-18.80^{+0.04}_{-0.05}$
beacon_0217-0509-12575	34.207989	−5.121376	28.4	28.0	$7.65^{+0.37}_{-0.37}$	$-18.81^{+0.04}_{-0.03}$
beacon_0217-0509-85	34.234711	−5.188540	28.0	27.6	$7.65^{+0.55}_{-0.46}$	$-19.28^{+0.05}_{-0.06}$
beacon_0217-0509-1420	34.225983	−5.182612	28.6	28.1	$7.66^{+0.70}_{-0.59}$	$-18.65^{+0.08}_{-0.09}$
beacon_1420+5252-12428	215.084641	52.882202	27.9	26.9	$7.70^{+0.05}_{-0.05}$	$-19.54^{+0.01}_{-0.01}$
beacon_0217-0508-3329	34.318546	−5.148247	28.4	28.8	$7.71^{+0.47}_{-0.44}$	$-18.73^{+0.05}_{-0.04}$
beacon_0217-0504-6193	34.273129	−5.037531	28.3	27.6	$7.72^{+0.50}_{-0.46}$	$-19.04^{+0.05}_{-0.04}$
beacon_0014-3025-6550	3.572950	−30.413603	…	28.8	$7.77^{+0.63}_{-0.62}$	$-17.97^{+0.06}_{-0.07}$
beacon_0217-0508-8355	34.290524	−5.122096	28.8	28.8	$7.81^{+0.52}_{-0.54}$	$-18.25^{+0.05}_{-0.05}$
beacon_0332-2745-9353	53.022465	−27.739815	28.9	28.5	$7.82^{+0.46}_{-0.50}$	$-18.32^{+0.04}_{-0.04}$
beacon_0332-2745-15255	53.043163	−27.734766	29.0	27.8	$7.83^{+0.78}_{-0.77}$	$-18.30^{+0.11}_{-0.09}$
beacon_0217-0508-8334	34.286720	−5.123929	29.5	29.2	$7.84^{+0.70}_{-0.67}$	$-17.68^{+0.06}_{-0.07}$
beacon_0217-0508-14393	34.269173	−5.105772	28.1	26.8	$7.88^{+0.39}_{-0.44}$	$-19.06^{+0.05}_{-0.08}$
beacon_0014-3025-14457	3.608568	−30.418518	…	25.8	$7.90^{+0.19}_{-0.48}$	$-21.17^{+0.02}_{-0.02}$
beacon_0332-2745-18704	53.035835	−27.718058	28.5	28.0	$7.90^{+0.69}_{-0.77}$	$-18.72^{+0.07}_{-0.09}$
beacon_0217-0509-9363	34.219463	−5.127748	27.9	26.9	$7.90^{+0.33}_{-0.52}$	$-19.36^{+0.04}_{-0.06}$
beacon_0217-0509-2346	34.244049	−5.167047	29.2	28.5	$7.94^{+0.81}_{-0.81}$	$-18.08^{+0.09}_{-0.13}$
beacon_0217-0504-15163	34.292065	−5.043071	27.8	27.8	$7.96^{+0.31}_{-0.38}$	$-19.39^{+0.04}_{-0.01}$

Table 2
(Continued)

ID	R.A.	Decl.	$m_{\rm F150W}$	$m_{\rm F444W}$	z	$M_{\rm UV}$
beacon_0217-0504-10020	34.314068	−5.089706	28.3	26.3	$7.99^{+0.74}_{-0.83}$	$-18.77^{+0.12}_{-0.16}$
beacon_0217-0508-3572	34.296047	−5.156882	28.1	27.9	$8.03^{+0.46}_{-0.58}$	$-19.12^{+0.05}_{-0.04}$
beacon_0217-0508-1995	34.301559	−5.166206	27.4	26.6	$8.06^{+0.34}_{-0.36}$	$-19.94^{+0.03}_{-0.03}$
beacon_0217-0504-3421	34.270123	−5.040110	27.6	26.9	$8.06^{+0.33}_{-0.78}$	$-19.57^{+0.05}_{-0.05}$
beacon_0014-3025-2599	3.553823	−30.410107	…	28.1	$8.07^{+0.37}_{-0.57}$	$-18.68^{+0.04}_{-0.03}$
beacon_0959+0200-8926	149.829056	2.021058	27.9	26.5	$8.10^{+0.35}_{-0.21}$	$-19.38^{+0.03}_{-0.02}$
beacon_1420+5252-11933	215.035583	52.892235	25.2	24.7	$8.12^{+0.11}_{-0.12}$	$-22.05^{+0.01}_{-0.01}$
beacon_0217-0509-1475	34.246601	−5.172431	28.0	27.9	$8.12^{+0.41}_{-0.83}$	$-19.19^{+0.05}_{-0.06}$
beacon_0014-3025-8648	3.613551	−30.434706	…	27.2	$8.18^{+0.25}_{-0.25}$	$-19.70^{+0.01}_{-0.01}$
beacon_1010+2701-2444	152.446686	26.987419	27.2	26.6	$8.23^{+0.66}_{-1.00}$	$-20.08^{+0.06}_{-0.13}$
beacon_0217-0509-9252	34.209660	−5.132755	29.4	28.5	$8.24^{+0.75}_{-0.93}$	$-17.82^{+0.07}_{-0.09}$
beacon_1010+2701-19789	152.471619	27.051905	28.0	27.6	$8.26^{+0.61}_{-0.93}$	$-19.22^{+0.05}_{-0.05}$
beacon_0332-2745-17578	53.037659	−27.711735	27.3	26.5	$8.27^{+0.29}_{-1.02}$	$-20.08^{+0.01}_{-0.21}$
beacon_0332-2749-18718	53.058949	−27.808054	27.1	26.3	$8.27^{+0.17}_{-0.19}$	$-20.29^{+0.01}_{-0.01}$
beacon_1010+2701-16958	152.464661	27.046890	27.8	27.5	$8.28^{+0.61}_{-1.04}$	$-19.40^{+0.05}_{-0.12}$
beacon_0332-2749-24726	53.001209	−27.802843	26.8	25.3	$8.29^{+0.12}_{-0.13}$	$-20.74^{+0.02}_{-0.01}$
beacon_0217-0504-3873	34.314297	−5.105042	28.9	28.5	$8.30^{+0.51}_{-0.86}$	$-18.34^{+0.05}_{-0.06}$
beacon_0332-2745-8569	53.053482	−27.765987	28.3	27.8	$8.35^{+0.35}_{-0.40}$	$-18.83^{+0.02}_{-0.02}$
beacon_0217-0509-1793	34.224037	−5.180541	27.9	26.1	$8.39^{+0.26}_{-0.22}$	$-19.50^{+0.01}_{-0.01}$
beacon_0332-2745-8259	53.050213	−27.764677	27.0	26.3	$8.40^{+0.54}_{-0.35}$	$-20.29^{+0.06}_{-0.05}$
beacon_0217-0509-336	34.223042	−5.191769	26.0	24.9	$8.41^{+0.13}_{-0.13}$	$-21.52^{+0.01}_{-0.01}$
beacon_0217-0508-1427	34.307549	−5.168149	27.9	27.5	$8.41^{+0.26}_{-0.32}$	$-19.40^{+0.03}_{-0.01}$
beacon_0332-2745-17579	53.037807	−27.711599	26.7	26.5	$8.41^{+0.21}_{-0.22}$	$-20.63^{+0.01}_{-0.01}$
beacon_0332-2745-9828	53.012547	−27.731163	27.0	26.1	$8.42^{+0.14}_{-0.14}$	$-20.34^{+0.01}_{-0.01}$
beacon_0217-0508-9685	34.272381	−5.125317	28.9	28.8	$8.45^{+0.38}_{-0.57}$	$-18.46^{+0.03}_{-0.04}$
beacon_0014-3025-11608	3.612495	−30.427191	…	27.2	$8.47^{+0.22}_{-0.26}$	$-19.39^{+0.01}_{-0.01}$
beacon_0217-0509-435	34.222919	−5.191683	28.3	27.2	$8.49^{+0.30}_{-1.15}$	$-19.19^{+0.01}_{-0.32}$
beacon_0217-0509-6946	34.211567	−5.140682	28.2	27.4	$8.52^{+0.38}_{-0.45}$	$-19.12^{+0.05}_{-0.01}$
beacon_0217-0504-24295	34.306004	−5.045831	28.9	28.0	$8.52^{+0.65}_{-0.75}$	$-18.43^{+0.06}_{-0.07}$
beacon_0217-0508-3135	34.317574	−5.149925	28.5	27.8	$8.54^{+0.33}_{-0.40}$	$-18.88^{+0.02}_{-0.02}$
beacon_0217-0509-14993	34.214493	−5.112545	27.4	27.4	$8.56^{+0.23}_{-0.30}$	$-19.88^{+0.01}_{-0.01}$
beacon_0217-0509-13335	34.218163	−5.103996	28.3	27.9	$8.59^{+0.30}_{-0.40}$	$-19.13^{+0.02}_{-0.01}$
beacon_0217-0504-3515	34.270214	−5.040026	27.7	26.7	$8.63^{+0.17}_{-0.19}$	$-19.79^{+0.01}_{-0.01}$
beacon_0332-2749-12382	53.087475	−27.814884	27.3	26.0	$8.64^{+0.12}_{-0.16}$	$-20.18^{+0.01}_{-0.01}$
beacon_0217-0508-9763	34.272213	−5.124932	26.6	26.1	$8.68^{+0.14}_{-0.12}$	$-20.86^{+0.01}_{-0.01}$
beacon_0447-2637-11548	71.671661	−26.582500	27.3	27.6	$8.73^{+0.33}_{-0.29}$	$-19.97^{+0.01}_{-0.03}$
beacon_0217-0508-8040	34.302929	−5.117467	28.1	27.8	$8.75^{+0.28}_{-0.30}$	$-19.29^{+0.02}_{-0.01}$
beacon_0217-0508-8415	34.292923	−5.120759	28.4	28.6	$8.77^{+0.31}_{-0.40}$	$-18.84^{+0.03}_{-0.01}$
beacon_0860+3857-14145	134.982574	38.985649	26.3	25.7	$8.79^{+0.19}_{-0.21}$	$-21.08^{+0.01}_{-0.01}$
beacon_0014-3025-10503	3.624762	−30.437508	…	27.0	$8.81^{+0.16}_{-0.17}$	$-20.22^{+0.01}_{-0.01}$
beacon_0217-0509-4602	34.220940	−5.160698	27.3	26.2	$8.82^{+0.25}_{-0.16}$	$-20.12^{+0.02}_{-0.01}$
beacon_1010+2701-420	152.422150	26.986328	26.0	24.7	$8.87^{+0.31}_{-0.25}$	$-21.44^{+0.04}_{-0.03}$
beacon_0217-0508-12114	34.277187	−5.113205	28.3	27.0	$8.92^{+0.25}_{-0.23}$	$-19.21^{+0.01}_{-0.01}$
beacon_0217-0509-11648	34.212341	−5.122705	27.7	27.2	$8.98^{+0.21}_{-0.20}$	$-19.57^{+0.01}_{-0.01}$
beacon_1420+5252-2768	215.008652	52.868328	26.4	26.4	$9.04^{+0.14}_{-0.15}$	$-21.05^{+0.01}_{-0.01}$
beacon_0217-0504-10016	34.283627	−5.044103	28.0	27.9	$9.07^{+0.24}_{-0.22}$	$-19.42^{+0.01}_{-0.01}$
beacon_0959+0200-16783	149.836929	2.041479	26.9	27.2	$9.14^{+0.17}_{-0.21}$	$-20.52^{+0.01}_{-0.01}$
beacon_0217-0504-7157	34.309956	−5.090462	26.9	27.7	$9.16^{+0.15}_{-0.15}$	$-20.28^{+0.01}_{-0.02}$
beacon_0217-0509-14115	34.200089	−5.116339	28.7	29.7	$9.25^{+0.09}_{-0.38}$	$-18.55^{+0.01}_{-0.01}$
beacon_1010+2701-18712	152.439987	27.060465	26.9	25.9	$9.31^{+1.60}_{-0.42}$	$-20.63^{+0.24}_{-0.10}$
beacon_0217-0508-1490	34.314037	−5.164579	28.3	28.1	$9.38^{+0.34}_{-0.55}$	$-19.25^{+0.01}_{-0.06}$
beacon_0217-0508-3296	34.305820	−5.154357	27.3	27.5	$9.40^{+0.28}_{-0.16}$	$-20.14^{+0.01}_{-0.01}$
beacon_0014-3025-13872	3.617229	−30.425524	…	26.0	$9.48^{+0.08}_{-0.08}$	$-21.69^{+0.01}_{-0.01}$
beacon_0217-0504-9016	34.283463	−5.046202	28.2	28.0	$9.52^{+1.32}_{-1.57}$	$-19.19^{+0.15}_{-0.52}$
beacon_0217-0509-2696	34.237087	−5.167516	27.6	27.2	$9.52^{+1.34}_{-1.46}$	$-19.82^{+0.15}_{-0.54}$
beacon_1010+2701-17114	152.439484	27.056280	26.5	26.0	$9.67^{+1.26}_{-0.22}$	$-21.42^{+0.07}_{-0.18}$
beacon_0332-2749-16743	53.001728	−27.812489	28.1	27.7	$9.79^{+0.57}_{-0.26}$	$-19.75^{+0.04}_{-0.01}$
beacon_0442-4613-8264	70.427460	−46.230682	26.2	26.9	$9.83^{+0.69}_{-0.99}$	$-21.02^{+0.04}_{-0.07}$

Table 2
(Continued)

ID	R.A.	Decl.	$m_{\rm F150W}$	$m_{\rm F444W}$	z	$M_{\rm UV}$
beacon_0217-0508-7634	34.305424	−5.118019	28.5	28.7	$9.91^{+0.78}_{-0.72}$	$-18.92^{+0.05}_{-0.06}$
beacon_0860+3857-10356	134.977585	38.971680	27.5	26.5	$9.99^{+1.22}_{-0.97}$	$-19.98^{+0.14}_{-0.18}$
beacon_0217-0509-12959	34.221210	−5.113707	29.0	28.6	$10.02^{+1.11}_{-1.03}$	$-18.62^{+0.08}_{-0.13}$
beacon_0217-0508-11070	34.298710	−5.107352	27.8	27.8	$10.04^{+0.61}_{-1.03}$	$-19.66^{+0.06}_{-0.07}$
beacon_0332-2749-19513	53.075996	−27.806505	27.8	28.0	$10.13^{+0.42}_{-0.43}$	$-19.74^{+0.01}_{-0.02}$
beacon_1138+5748-2321	174.362198	57.776512	27.1	26.3	$10.17^{+1.36}_{-1.31}$	$-20.52^{+0.15}_{-0.15}$
beacon_0332-2749-17529	53.085506	−27.808601	27.7	28.0	$10.24^{+0.67}_{-0.62}$	$-19.90^{+0.03}_{-0.04}$
beacon_0217-0509-13052	34.221394	−5.113218	28.1	28.4	$10.26^{+0.45}_{-0.61}$	$-19.49^{+0.04}_{-0.02}$
beacon_0217-0509-11058	34.217091	−5.122624	28.7	27.3	$10.32^{+1.12}_{-1.11}$	$-18.84^{+0.13}_{-0.17}$
beacon_1010+2701-12141	152.432724	27.044855	28.4	26.7	$10.75^{+0.98}_{-1.30}$	$-19.34^{+0.12}_{-0.08}$
beacon_0959+0200-14138	149.845947	2.032689	28.2	27.5	$11.04^{+0.44}_{-0.38}$	$-19.57^{+0.03}_{-0.01}$
beacon_0332-2745-18596	53.085110	−27.757654	28.2	27.8	$11.22^{+0.70}_{-0.70}$	$-20.07^{+0.04}_{-0.04}$
beacon_0332-2749-6608	53.005013	−27.824554	29.3	27.8	$12.29^{+2.46}_{-1.19}$	$-19.64^{+0.24}_{-0.14}$

Note. Sources are sorted in increased order of redshift.

Limiting magnitudes, calculated for a fixed aperture size, are listed.

Some fields overlap with previous extragalactic JWST fields, including A2744 (T. Treu et al. 2022; I. Labbe et al. 2025), COSMOS (C. M. Casey et al. 2023), AEGIS (M. B. Bagley et al. 2023), UDS (C. T. Donnan et al. 2024), and GOODS-South/North (K. N. Hainline et al. 2024). As mentioned previously, in those overlapping fields we supplement the filters that were not previously used (especially F090W; and when possible use medium filters such as F140M/F182M/F210M/F430M/F480M), to enable searches of emission line galaxies at $7 < z < 9$ and improve photometric-redshift accuracy.

5.2. Identification of z > 7 galaxies

From the DR1 fields, we have identified 129 galaxy candidates at $z > 7$, consisting of 118 F090W dropouts, 11 F115W dropouts, and 0 F150W dropouts. In Figure 6, we show the redshift–$M_{\rm UV}$ distribution of the selected sources (Table 2). The faint end of the UV magnitude probed here is ~ -18 mag, consistent with the prediction by the exposure time calculator. We observe several luminous (<-21 mag) galaxies at $8 < z < 10$. As we see below (Section 5.3), the observed number of those luminous galaxies is overall consistent with pre-JWST studies (e.g., R. J. Bouwens et al. 2015; M. Stefanon et al. 2019), post-JWST (G. C. K. Leung et al. 2023; C. J. Willott et al. 2024), and also theoretical predictions (e.g., C. A. Mason et al. 2023).

On the other hand, at $z > 10$ we do not find many luminous galaxies that are comparable to GN-z11 (P. A. Oesch et al. 2018; A. J. Bunker et al. 2023; S. Tacchella et al. 2023), GHZ2 (M. Castellano et al. 2022; R. P. Naidu et al. 2022), and JADES-GS-z14-0 (S. Carniani et al. 2024). Also shown in Figure 6 are spec-z confirmed sources in the literature. Interestingly, while the total area of the Beacon DR1 is comparable to those in the literature, we seem to be lacking luminous (<-20 mag) galaxies at $z > 10$, casting doubt on our selection being too conservative. However, we confirmed that our color selection would successfully reproduce 12 of the 13 sources at $z_{\rm spec} > 10$. The only unsuccessful case (GS-z10-0; E. Curtis-Lake et al. 2023) is a faint galaxy ($m_{200} \sim 29$ mag) and thus our phot-z estimate has large error bars ($z_{\rm phot} = 2.5^{+8.8}_{-2.2}$ at 1σ). Given the high success rate of our color selection, we suspect that the difference in $z > 10$ galaxy number densities may originate in cosmic variance. In fact, six and three of the $z_{\rm spec} > 10$ sources are located in the GOODS-South field and *one* CEERS pointing, respectively. A further investigation of cosmic variance will be presented in our future work (K. Kreilgaard 2025, in preparation).

5.2.1. Overview of Individual High-z Galaxy Candidates

In the redshift range of $z < 10$, we show two example candidates selected within the F090W dropout window. These examples are representative for UV luminous galaxies and yet show different spectral features: ID336 is UV-bright ($M_{\rm UV} = -21.5$), best fitted with an extreme emission line template, characterized by a blue rest-frame UV slope ($\beta = -1.9 \pm 0.1$), and flux excess in the F444W band. By attributing the F444W flux excess to strong Hβ+[O III] emission, we obtain rest-frame equivalent width EW$_0$(Hβ + O III) $\sim$ 2300 Å (see P. Rinaldi et al. 2023). The other example source, ID2768, is located in the field beacon_1420+5252, where several medium bands are also taken (F140M, F182M, F410M, F430M, F480M). Red medium-band filters sample the wavelength around the Balmer break and thus effectively discriminate other possible solutions, e.g., line excess due to strong Hβ+[O III] emission lines, as seen in ID336.

We have identified 11 $z \gtrsim 10$ galaxies of moderate brightness, $-M_{\rm UV} \sim 18.5$–20.5, from the F115W dropout selection. Although the photometric flux errors are relatively large, leading to larger z uncertainties, all of these candidates are secured with a clear dropout in the F090W and F115W bands. At $z > 9$, Hβ+[O III] lines are redshifted to >5 μm and thus a relatively flat slope is expected at $\sim$2–5 μm. In Figure 7, we show two example sources from this redshift. ID13052 has a secondary solution at $z \sim 2.4$. The existing photometry, however, at $\sim$1.5 μm discriminates the low-z solution. ID6608 is one of the highest-redshift candidates among our final sample. It has a relatively wide redshift probability distribution at $z > 10$, which is partially attributed to the fact that the spectrum is rather featureless for the observed wavelength range. However, the redshift probability at $z < 10$, with a secondary solution at $z \sim 3.6$, is low ($p(z < 10) = 0.004$), making it still qualified as a high-z candidate. This source is characterized with a moderately blue UV slope, $\beta_{\rm UV} = -2.5 \pm 0.1$. The light-weighted stellar age

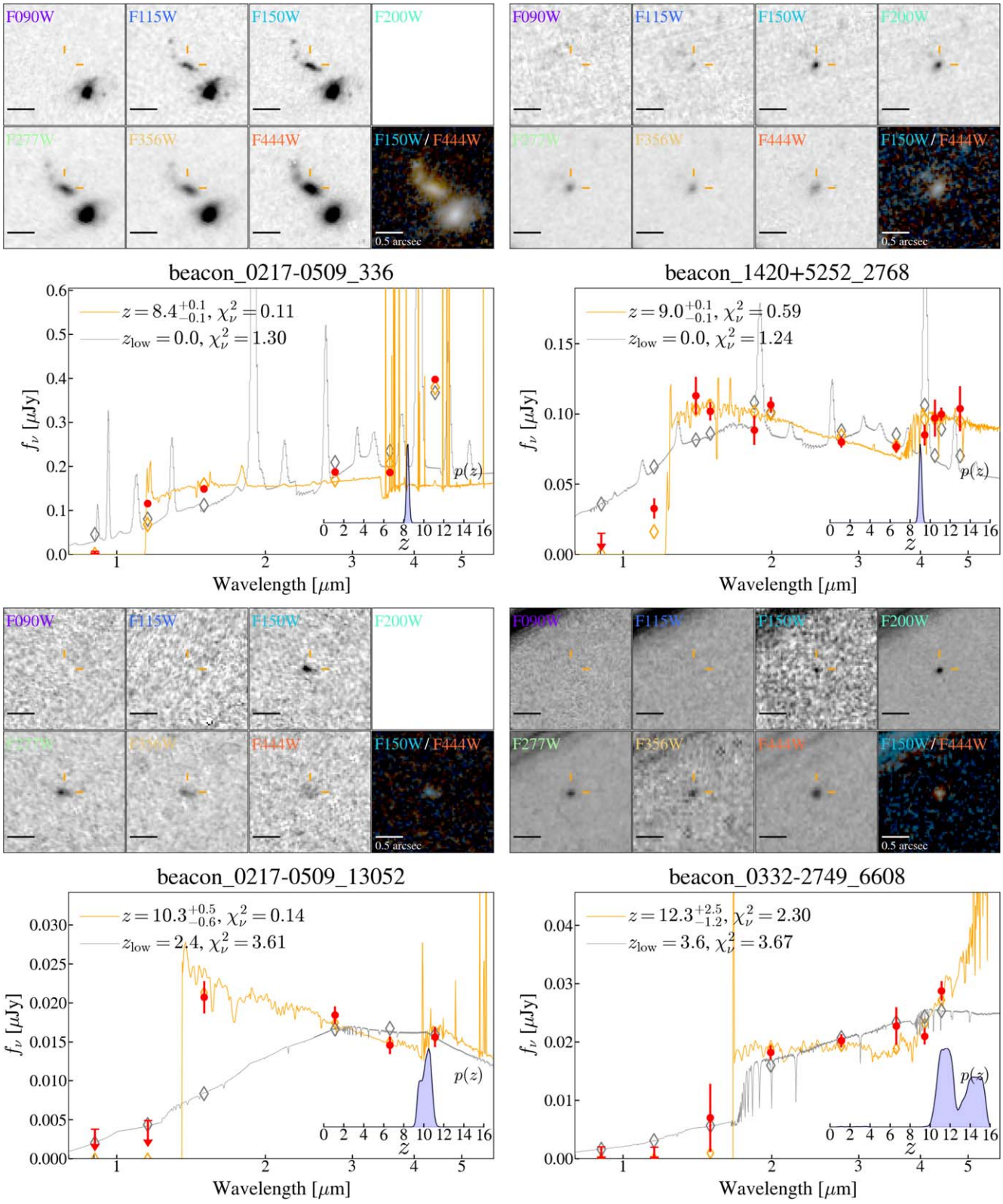

Figure 7. Postage stamps and SEDs of example high-z galaxy candidates. The best-fit flux models at high redshift (orange lines) and at the secondary low redshift ($z_{\rm low}$, gray line) are shown. Photometric redshift probability distributions derived from EAzY are shown in the inset. The y-axis is set in a linear scale.

from our SED fitting analysis is $t \sim 10$ Myr, suggesting the dominance of young stellar populations. The other example, ID6608 at $z \sim 12.3$, on the other hand shows a redder UV slope (-1.8), consisting of more evolved populations $t \sim 100$ Myr.

Also noted is that most of the selected candidates have extended morphologies. While the multiband NIRCam filters up to $\sim$5 μm effectively eliminates the contamination of foreground low-mass stars (see Section 5.4), the morphological

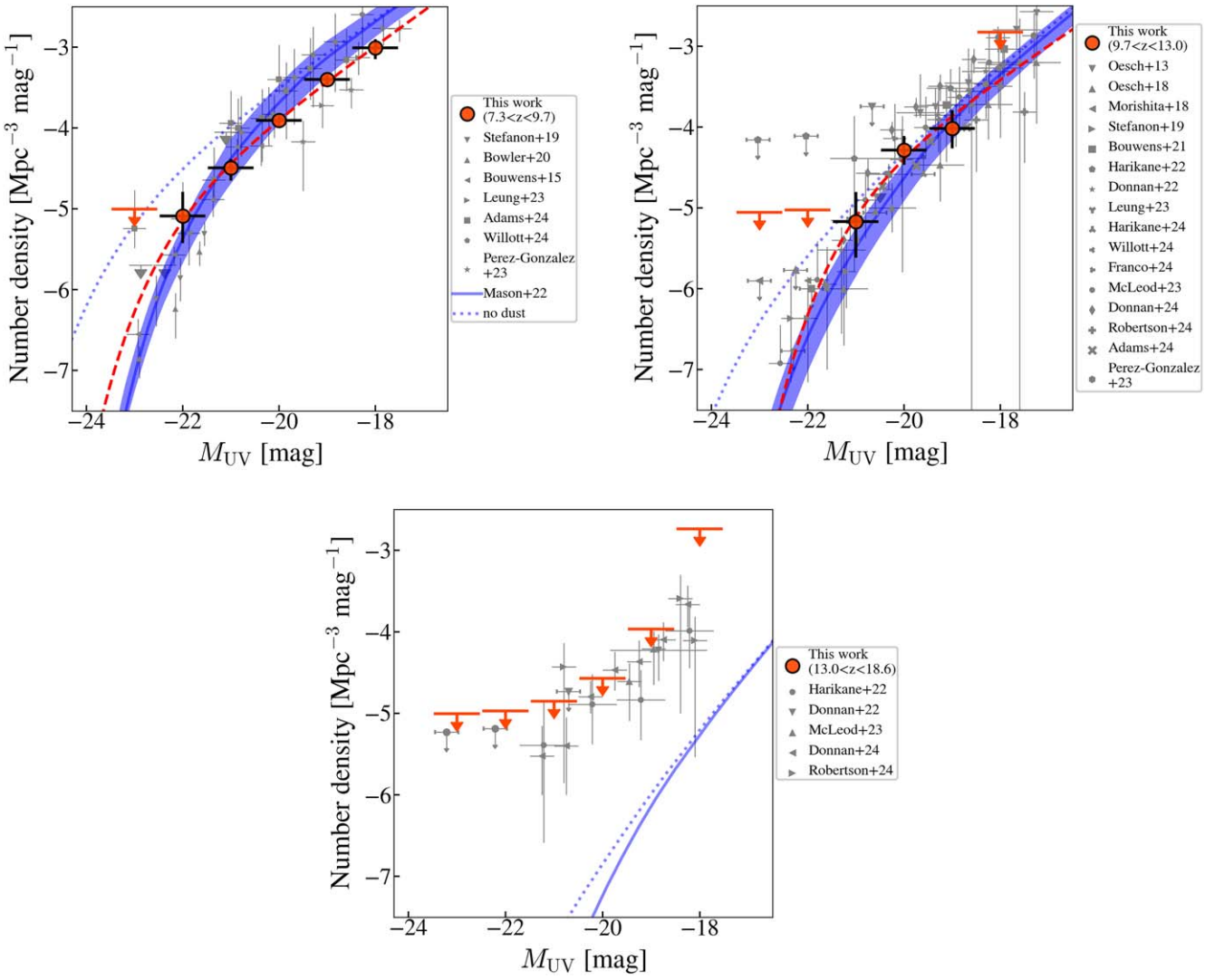

Figure 8. Number densities estimated for the Beacon DR1 sources (red circles and upper limits), at $z \sim 8.5$ (left top), $z \sim 11$ (right top), and $z \sim 15$ (bottom). For magnitude bins without any sources, we show 2σ upper limits. The Schechter fit to our number density estimates is shown (red dashed lines). Number density estimates in the literature are shown (gray symbols; P. A. Oesch et al. 2013; R. J. Bouwens et al. 2015, 2021; T. Morishita et al. 2018; M. Stefanon et al. 2019; C. T. Donnan et al. 2023; Y. Harikane et al. 2023, 2024; G. C. K. Leung et al. 2023; P. G. Pérez-González et al. 2023; N. J. Adams et al. 2024; M. Franco et al. 2024; D. J. McLeod et al. 2024; S. Rojas-Ruiz et al. 2024; C. J. Willott et al. 2024). The C. A. Mason et al. (2023) LFs (blue solid lines for the dust model, dashed lines for the no-dust model) of the corresponding redshift are shown. The redshift variation of the dust model is shown by a hatched region.

information (e.g., size, elongation, light concentration) of the color-selected source can further secure the final sample selection (Y. Zhang 2025, in preparation).

5.3. Number Densities of UV-selected Galaxies at z > 7

Using the selected candidates, we aim to estimate the number density of galaxies at $z > 7$. An unusual aspect of our survey is that each field has different depths and filters. This results in completeness and selection functions that vary from field to field, requiring a careful effective volume estimate in each field.

For the effective volume estimate, we use an adaptation of the `GLACiAR2` completeness simulation code (N. Leethochawalit et al. 2023a, 2023b). Briefly, in each field, we inject 1200 galaxies into each magnitude–redshift bin. The bins run from $z = 6$ to 18 and from $M_{UV} = -18.5$ to -24 mag with an increment of 0.5 in both directions. The injected galaxies are assumed to have a Sérsic profile of $n = 1$ with the sizes that follow the $M_{\rm UV}$–size relation as a function of the redshift in T. Morishita et al. (2024). The spectral shapes of the galaxies are randomly pulled from the JAGUAR (C. C. Williams et al. 2018) catalogs of the same redshift bin up to $z = 12$. Since there are not many spectra at $z > 12$ in the JAGUAR catalog, we combine all $z > 12$ JAGUAR spectra into one spectral pool. The images of the injected galaxies are convolved with the PSF from the F444W band and injected into the PSF-matched images. The detection, photometric extraction, and sample selection of the injected galaxies are done in the same manner as the real sources.

We then calculate the effective volume of each field as in N. Leethochawalit et al. (2023a):

$$V_{\rm eff}(M_{\rm recov}) = \int \frac{dV}{dz} P(M_{\rm recov}, z) dz. \quad (1)$$

ff$P(M_{\rm recov}, z)$ is the number of simulated galaxies at redshift z that are recovered to have UV magnitude in the bin $M_{\rm recov}$ (regardless of their intrinsic UV magnitude), divided by the number of injected galaxies at redshift z with intrinsic UV magnitude equal to $M_{\rm recov}$. For reference, at the brightest

Table 3
Number Density of Galaxies at $z > 8$

$M_{\rm UV}$ (mag)	Volume[a] (10^3 Mpc^3)	$N_{\rm obj}$	Number Density[b] (log Mpc^{-3} mag^{-1})
	F090W dropout		
−23.0	366.9	0	<-5.30
−22.0	366.5	3	$-5.09^{+0.34}_{-0.29}$
−21.0	344.6	11	$-4.50^{+0.16}_{-0.11}$
−20.0	282.0	33	$-3.93^{+0.08}_{-0.07}$
−19.0	143.0	54	$-3.42^{+0.06}_{-0.06}$
−18.0	13.3	13	$-3.01^{+0.14}_{-0.11}$
−17.0	0.1	0	<-1.74
	F115W dropout		
−23.0	394.4	0	<-5.33
−22.0	365.1	0	<-5.30
−21.0	276.2	2	$-5.14^{+0.45}_{-0.36}$
−20.0	152.2	8	$-4.28^{+0.18}_{-0.17}$
−19.0	52.1	5	$-4.02^{+0.24}_{-0.22}$
−18.0	2.4	0	<-3.13
−17.0	0.1	0	<-1.64
	F150W dropout		
−23.0	355.7	0	<-5.29
−22.0	328.1	0	<-5.25
−21.0	249.3	0	<-5.14
−20.0	133.3	0	<-4.86
−19.0	33.9	0	<-4.27
−18.0	2.0	0	<-3.04
−17.0	0.1	0	<-1.89

Notes.
[a] Effective volume calculated by the completeness simulation.
[b] 1σ uncertainty calculated for small number statistics as in N. Gehrels (1986).

magnitude bins (i.e., ∼100% completeness), the effective volumes for a single NIRCam pointing are approximately 2×10^4 Mpc^3 for all redshift windows. Once effective volumes are calculated, we calculate the number density at each absolute UV magnitude bin by combining all fields.

The estimated galaxy number densities are shown in Figure 8. Our estimates are overall consistent with studies in the literature at $7 < z < 13$ (R. Bouwens et al. 2023; C. T. Donnan et al. 2023; Y. Harikane et al. 2023; C. M. Casey et al. 2024; N. J. Adams et al. 2024; M. Franco et al. 2024; C. J. Willott et al. 2024). Our estimates are also consistent with the theoretical prediction of C. A. Mason et al. (2023). The total effective volumes and the calculated number densities are listed in Table 3.

To assess our results in more detail, we fit the number density estimates with the P. Schechter (1976) function:

$$\phi(M_{\rm UV}) = \frac{\ln 10}{2.5}\phi^* \times 10^{-0.4(\alpha+1)(M_{\rm UV}-M^*)} \times \exp[-10^{-0.4(M_{\rm UV}-M^*)}] \quad (2)$$

using a Markov Chain Monte Carlo method (e.g., T. Morishita et al. 2018). The derived parameters for the $7.3 < z < 9.7$ number density are $\alpha = -2.07^{+0.23}_{-0.18}$, $\log \phi^* = -4.66^{+0.53}_{-0.44}$, and $M^* = -21.97^{+0.73}_{-0.66}$. For the $9.7 < z < 13$ range, we fix the slope to $\alpha = -2$ and find $\log \phi^* = -4.57^{+2.10}_{-0.96}$ and $M^* = -21.01^{+1.61}_{-1.45}$.

We estimate that we will find ∼650 galaxies at $7.3 < z < 9.7$ and ∼100 at $9.7 < z < 13$ in the full BEACON data set, by using our LF estimates and simply scaling the survey volume while assuming 80% completeness down to the 10σ limiting magnitude. Our LF predicts similar numbers of galaxies to those of the constant star formation efficiency model by C. A. Mason et al. (2023) as in Figure 2.

Despite covering a considerably large total area (∼180 arcmin^2), there are no $z > 13$ galaxy candidates selected in our final samples. We place upper limits for the number densities (Figure 8). The upper limits derived are still consistent with previous studies in legacy fields (Y. Harikane et al. 2023; C. T. Donnan et al. 2024; D. J. McLeod et al. 2024), except for B. Robertson et al. (2024) at the bright end ($M_{\rm UV} \sim -21$), which contains the luminous $z = 14$ galaxy GS-z14-0. The absence of luminous $z > 13$ galaxies in our fields may suggest a significant impact from cosmic variance affecting the statistics in those legacy fields. As we see in Section 5.1, a large fraction of $z_{\rm spec} > 10$ sources are located just in *two* fields. In addition, exceptionally luminous sources in the literature (GN-z11, GHZ2/GLASS-z12, GS-z14-0) are found in fields of relatively high cosmic variance ($\sigma_{\rm cv} > 0.4$; Figure 1). The complete data set of BEACON will reach a 5× larger volume (∼1.5×10^6 Mpc^3) and facilitate us to explore this further.

5.4. Ancillary Science

Our pure-parallel survey will provide a unique and extensive data set for legacy science at lower redshifts. In particular, our filter coverage can secure key spectral features, such as the Balmer break of $z \sim 2$ galaxies (Figure 3) and the 3.3 μm PAH emission line of $z \sim 0.3$ galaxies seen as a flux excess in F410M (e.g., B. Vulcani et al. 2023). In Figure 9, we show two galaxy examples selected from the DR1 fields: a passively evolving galaxy at $z \sim 1.9$ and a dusty galaxy at $z \sim 4$. Also, foreground low-mass stars (brown dwarfs) are often found as contaminants in high-z galaxy color selection, for their similar spectral features, i.e., the color break at observed ∼1 μm (T. Morishita et al. 2020; Y. Ishikawa et al. 2022, also J. E. Greene et al. 2024 for spectroscopic confirmation of faint brown dwarf stars). The NIRCam data from BEACON securely discriminate those stars from galaxy populations by adding longer wavelength data points at >2 μm. The secure selection of faint stars enables us to study, e.g., their spatial distribution in the Milky Way halo (e.g., R. E. Ryan et al. 2011; B. W. Holwerda et al. 2014). In Figure 9, we show one M-dwarf candidate, selected from spectral template fitting using the SPEX library (J. T. Rayner et al. 2003) and additional morphological analysis for point-source selection.

Lastly, we expect some fraction of our fields to overlap with the existing survey fields where previous NIRCam fields are available. This is because long-exposure spectroscopic observations tend to target sources found within those popular legacy fields. In the DR1 fields, seven are found within the legacy fields (Figure 4). Those overlapping fields are ideal for the detection of transient events and variability studies (e.g., M. Kokubo & Y. Harikane 2024; Z. Zhang et al. 2024).

6. Summary

In this paper, we introduced BEACON, a new pure-parallel imaging survey scheduled in JWST Cycle 2. Using the first 19 fields, we established our data reduction processes and

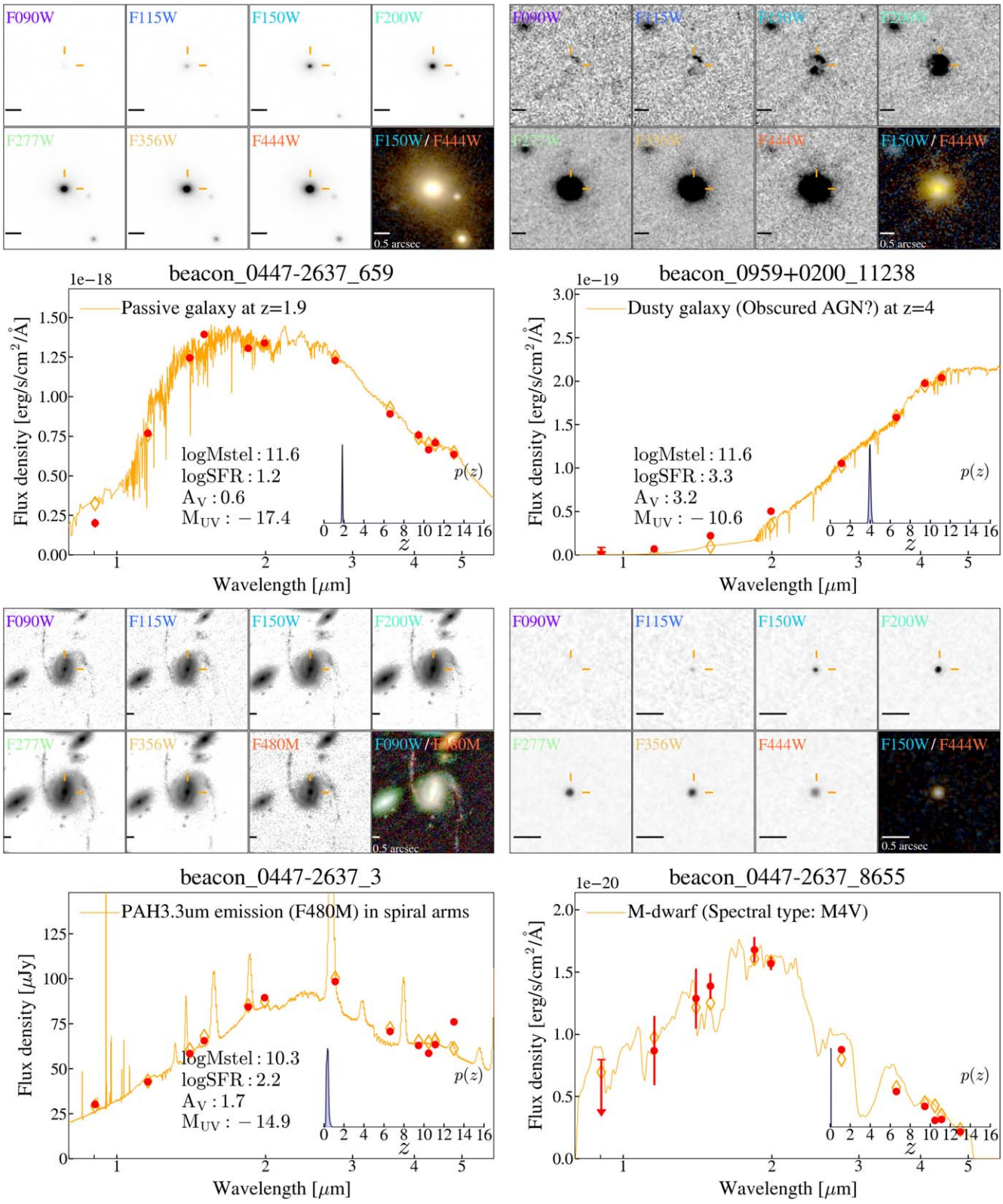

Figure 9. Examples of low-z sources from BEACON. The figure format is the same as in Figure 7. Top left: Massive ($\log M^*/M_\odot \sim 11.6$), passively evolving galaxy at $z \sim 1.9$. Top right: Dusty galaxy at $z \sim 4$. The galaxy is characterized by a red spectral shape ($A_V \sim 3.2$). It has a compact point source (possibly obscured AGN) dominating at >2 μm, whereas extended structures are seen in bluer wavelengths. Bottom left: $z \sim 0.45$ spiral galaxy, with the flux excess in F480M, corresponding to the 3.3 μm PAH line. Bottom right: faint ($m_{\rm F200W} = 25.6$), M4V dwarf selected from point-source analysis and spectral template fitting. The best-fit spectral template (M4V) from the SPEX library (yellow line) is shown.

performed an initial high-z galaxy search. Through our careful color selection utilizing 6–8+ NIRCam filters, we identified 129 galaxy candidates at $7 < z < 13$. The galaxy number densities estimated in the fields are overall consistent with the previous estimates in the literature. Although our exploration reached a considerably large area ($\sim$180 arcmin^2), we found

Table 4
Columns and Description for the Photometric Catalogs

Column	Unit	Description
		Photometric Catalog
id		Individual identification name of objects
ra	degree	R.A. (J2000).
dec	degree	decl. (J2000).
x	pixel	x position in image coordinate.
y	pixel	y position in image coordinate.
f_family xx	f_ν	Total flux of objects in band family xx.
e_family xx	f_ν	Flux error (1σ) in the total flux of objects in band family xx.
flux_iso_family xx	f_ν	Isophotal flux in band family xx.
fluxerr_iso_family xx	f_ν	Flux error (1σ) in isophotal flux in band family xx.
flux_aper_family n_family xx	f_ν	Aperture flux in band family xx in the family nth aperture. Aperture diameter sizes are: [0.16, 0.32, 0.48, 0.64, 1.28, 2.56] arcsec.
flux_aper_family n_family xx	f_ν	Flux error (1σ) in aperture flux in band family xx in the family nth aperture.
flag_family xx		SExtractor photometry flag for band family xx.
kron_radius_family xx	pixel	Kron radius in band family xx.
a_image_family xx	pixel	Radius along the major axis in band family xx.
b_image_family xx	pixel	Radius along the minor axis in band family xx.
theta_family xx	degree	SExtractor position angle in band family xx measured counterclockwise.
class_star_family xx		SExtractor class star indicator in band family xx.
flux_radius_family xx	pixel	SExtractor nonparametric half-light radius in band family xx.
flux_scale		Scale ratio of total flux to aperture flux measured in the detection band. The minimum scale is set to 1.
		Redshift catalog
zfamily n		Photometric redshift at the family nth percentile of the redshift likelihood distribution.
zpeak		Photometric redshift at the peak of global likelihood redshift distribution.
chi2		Reduced chi-square at zpeak.
MUVfamily n	mag	Absolute UV (1450 Å) magnitude calculated at zfamily n.
MUVpeak	mag	Absolute UV (1450 Å) magnitude calculated at zpeak.
plow		Total probability of redshift distribution at $z <$ zset.
phigh		Total probability of redshift distribution at $z >$ zset.
UVbeta_lambda		UV-beta slope (β_λ) calculated with the best-fit template at zpeak.
U-V	mag	Rest-frame $U - V$ color calculated with the best-fit template at zpeak.
B-V	mag	Rest-frame $B - V$ color calculated with the best-fit template at zpeak.
V-J	mag	Rest-frame $V - J$ color calculated with the best-fit template at zpeak.
z-J	mag	Rest-frame $z - J$ color calculated with the best-fit template at zpeak.
z_peak_low		Photometric redshift at the peak of redshift likelihood distribution at $z < z_{\rm set}$.
chi2_peak_low		Reduced chi-square at z_peak_low.
z_peak_high		Photometric redshift at the peak of redshift likelihood distribution at $z > z_{\rm set}$.
chi2_peak_high		Reduced chi-square at z_peak_high.
nfilt		Number of filters used for photometric redshift fit.

Note. All fluxes are corrected for the Galactic dust extinction, and set to magnitude zero-point of $m_0 = 25$, i.e., $m = -2.5\log(f_\nu) + m_0$. For sources with filters without data coverage, the flux error arrays are set to -99.

zero $z > 13$ galaxies. However, the upper limits of the $z > 13$ galaxy number density are consistent with previous studies in the literature. Further exploration utilizing the full BEACON data set will confidently determine the contribution of cosmic variance to the number densities of bright $z > 13$ galaxies detected so far with JWST.

The BEACON data set also allows for a range of lower-z science cases, such as the search for massive galaxies at cosmic noon and foreground low-mass stars. We plan to process all imaging data and publish the resulting products, including photometric flux redshift catalogs for each survey field. We will also make available the effective volume estimate from our completeness simulation. We will publish the data products of the DR1 fields on a dedicated website. Catalog data models are presented in Table 4. The full data release will be made when the program is complete.

Acknowledgments

We thank the program coordinators of our JWST program, Shelly Meyett and Blair Porterfield, and the instrument scientist, Anton Koekemoer, for their invaluable assistance in configuring our observations. In addition to being one of the largest JWST programs, the complexity of the pure-parallel mode introduced a series of unique challenges and issues, each of which benefited greatly from their expertise and perspectives. We also thank the Cycle 1 and 2 pure-parallel program teams (PASSAGE, PANORAMIC, and PID 3383 (PI Glazebrook)) for their pioneering efforts, which laid the essential foundation and facilitated the operation of pure-parallel observations. We thank Xuejian Shen (MIT) and the THESAN team for sharing dark-matter density maps and related physical property catalogs from their simulations. T.M. and Y.Z. thank George Helou for the support in our data analysis at IPAC. We

thank the anonymous referee for the careful reading of the manuscript and constructive comments. Support for program 3990 was provided by NASA through the Space Telescope Science Institute, which is operated by the Association of Universities for Research in Astronomy, Inc., under NASA contract NAS 5-03127. All of the data presented in this paper were obtained from the Mikulski Archive for Space Telescopes (MAST) at the Space Telescope Science Institute. The specific observations analyzed can be accessed via DOI:10.17909/q8cd-2q22. C.A.M., K.C.K., and V.G. acknowledge support from the Carlsberg Foundation under grant CF22-1322. The Cosmic Dawn Center (DAWN) is funded by the Danish National Research Foundation under grant DNRF140. B.V. acknowledges support from the European Union—NextGenerationEU RFF M4C2 1.1 PRIN 2022 project 2022ZSL4BL INSIGHT. M.B. acknowledges support from the ERC Grant FIRSTLIGHT and Slovenian national research agency ARIS through grants N1-0238 and P1-0188. T.M. received support from NASA through the STScI grants HST-GO-17231 and JWST-GO-1747.

Software: AstroML (J. Vanderplas et al. 2012), Astropy (Astropy Collaboration et al. 2013, 2018, 2022), bbpn (T. Morishita 2023), EAzY (G. B. Brammer et al. 2008), EMCEE (D. Foreman-Mackey et al. 2013), numpy (C. R. Harris et al. 2020).

ORCID iDs

Takahiro Morishita https://orcid.org/0000-0002-8512-1404
Charlotte A. Mason https://orcid.org/0000-0002-3407-1785
Kimi C. Kreilgaard https://orcid.org/0009-0005-9953-433X
Michele Trenti https://orcid.org/0000-0001-9391-305X
Tommaso Treu https://orcid.org/0000-0002-8460-0390
Benedetta Vulcani https://orcid.org/0000-0003-0980-1499
Yechi Zhang https://orcid.org/0000-0003-3817-8739
Abdurro'uf https://orcid.org/0000-0002-5258-8761
Anahita Alavi https://orcid.org/0000-0002-8630-6435
Hakim Atek https://orcid.org/0000-0002-7570-0824
Yannick Bahé https://orcid.org/0000-0002-3196-5126
Maruša Bradač https://orcid.org/0000-0001-5984-0395
Larry D. Bradley https://orcid.org/0000-0002-7908-9284
Dan Coe https://orcid.org/0000-0001-7410-7669
James Colbert https://orcid.org/0000-0001-6482-3020
Viola Gelli https://orcid.org/0000-0001-5487-0392
Matthew J. Hayes https://orcid.org/0000-0001-8587-218X
Tucker Jones https://orcid.org/0000-0001-5860-3419
Tadayuki Kodama https://orcid.org/0000-0002-2993-1576
Nicha Leethochawalit https://orcid.org/0000-0003-4570-3159
Zhaoran Liu https://orcid.org/0009-0002-8965-1303
Matthew A. Malkan https://orcid.org/0000-0001-6919-1237
Vihang Mehta https://orcid.org/0000-0001-7166-6035
Benjamin Metha https://orcid.org/0000-0002-8632-6049
Andrew B. Newman https://orcid.org/0000-0001-7769-8660
Marc Rafelski https://orcid.org/0000-0002-9946-4731
Guido Roberts-Borsani https://orcid.org/0000-0002-4140-1367
Michael J. Rutkowski https://orcid.org/0000-0001-7016-5220
Claudia Scarlata https://orcid.org/0000-0002-9136-8876
Massimo Stiavelli https://orcid.org/0000-0001-9935-6047
Ryo A. Sutanto https://orcid.org/0009-0005-1487-7772
Kosuke Takahashi https://orcid.org/0009-0009-8116-0316
Harry I. Teplitz https://orcid.org/0000-0002-7064-5424
Xin Wang https://orcid.org/0000-0002-9373-3865

References

Adams, N. J., Conselice, C. J., Austin, D., et al. 2024, ApJ, 965, 169
Arrabal Haro, P., Dickinson, M., Finkelstein, S. L., et al. 2023, ApJL, 951, L22
Astropy Collaboration, Price-Whelan, A. M., Lim, P. L., et al. 2022, ApJ, 935, 167
Astropy Collaboration, Price-Whelan, A. M., Sipőcz, B. M., et al. 2018, AJ, 156, 123
Astropy Collaboration, Robitaille, T. P., Tollerud, E. J., et al. 2013, A&A, 558, A33
Atek, H., Siana, B., Scarlata, C., et al. 2011, ApJ, 743, 121
Bagley, M. B., Finkelstein, S. L., Koekemoer, A. M., et al. 2023, ApJL, 946, L12
Bagley, M. B., Pirzkal, N., Finkelstein, S. L., et al. 2024, ApJL, 965, L6
Barro, G., Faber, S. M., Koo, D. C., et al. 2017, ApJ, 840, 47
Barrufet, L., Oesch, P., Marques-Chaves, R., et al. 2025, MNRAS, 537, 3453
Behroozi, P., Wechsler, R., Hearin, A., & Conroy, C. 2019, MNRAS, 488, 3143
Bernard, S. R., Carrasco, D., Trenti, M., et al. 2016, ApJ, 827, 76
Bertin, E., & Arnouts, S. 1996, A&AS, 117, 393
Bezanson, R., Labbe, I., Whitaker, K. E., et al. 2024, ApJ, 974, 92
Bhowmick, A. K., Somerville, R. S., Di Matteo, T., et al. 2020, MNRAS, 496, 754
Boucaud, A., Bocchio, M., Abergel, A., et al. 2016, A&A, 596, A63
Bouwens, R., Illingworth, G., Oesch, P., et al. 2023, MNRAS, 523, 1009
Bouwens, R. J., Illingworth, G. D., Oesch, P. A., et al. 2010, ApJL, 709, L133
Bouwens, R. J., Illingworth, G. D., Oesch, P. A., et al. 2015, ApJ, 803, 34
Bouwens, R. J., Oesch, P. A., Stefanon, M., et al. 2021, AJ, 162, 47
Bouwens, R. J., Stefanon, M., Oesch, P. A., et al. 2019, ApJ, 880, 25
Bowler, R. A. A., Dunlop, J. S., McLure, R. J., et al. 2014, MNRAS, 440, 2810
Bowler, R. A. A., Jarvis, M. J., Dunlop, J. S., et al. 2020, MNRAS, 493, 2059
Boylan-Kolchin, M. 2023, NatAs, 7, 731
Bradley, L. 2023, larrybradley/lacosmic: v1.1.0, Zenodo, doi:10.5281/zenodo.10145563
Bradley, L. D., Trenti, M., Oesch, P. A., et al. 2012, ApJ, 760, 108
Brammer, G. B., van Dokkum, P. G., & Coppi, P. 2008, ApJ, 686, 1503
Brammer, G., Strait, V., Matharu, J., & Momcheva, I. 2022, grizli, v1.5.0, Zenodo, doi:10.5281/zenodo.6672538
Bridge, J. S., Holwerda, B. W., Stefanon, M., et al. 2019, ApJ, 882, 42
Brinch, M., Greve, T. R., Weaver, J. R., et al. 2023, ApJ, 943, 153
Bunker, A. J., Saxena, A., Cameron, A. J., et al. 2023, A&A, 677, A88
Bunker, A. J., Stanway, E. R., Ellis, R. S., & McMahon, R. G. 2004, MNRAS, 355, 374
Bunker, A. J., Wilkins, S., Ellis, R. S., et al. 2010, MNRAS, 409, 855
Burgasser, A. J., Bezanson, R., Labbe, I., et al. 2024, ApJ, 962, 177
Calvi, V., Trenti, M., Stiavelli, M., et al. 2016, ApJ, 817, 120
Cameron, A. J., Trenti, M., Livermore, R. C., & van der Velden, C. 2019, MNRAS, 483, 1922
Cardelli, J. A., Clayton, G. C., & Mathis, J. S. 1989, ApJ, 345, 245
Carnall, A. C., McLeod, D. J., McLure, R. J., et al. 2023, MNRAS, 520, 3974
Carnall, A. C., McLure, R. J., Dunlop, J. S., et al. 2023, Natur, 619, 716
Carniani, S., Hainline, K., D'Eugenio, F., et al. 2024, Natur, 633, 318
Casertano, S., de Mello, D., Dickinson, M., et al. 2000, AJ, 120, 2747
Casey, C. M., Akins, H. B., Shuntov, M., et al. 2024, ApJ, 965, 98
Casey, C. M., Kartaltepe, J. S., Drakos, N. E., et al. 2023, ApJ, 954, 31
Castellano, M., Fontana, A., Treu, T., et al. 2022, ApJL, 938, L15
Castellano, M., Napolitano, L., Fontana, A., et al. 2024, ApJ, 972, 143
Chabrier, G. 2003, PASP, 115, 763
Chartab, N., Mobasher, B., Darvish, B., et al. 2020, ApJ, 890, 7
Chen, Z., Stark, D. P., Endsley, R., et al. 2023, MNRAS, 518, 5607
Conroy, C., Gunn, J. E., & White, M. 2009, ApJ, 699, 486
Conselice, C. J., Basham, J. T. F., Bettaney, D. O., et al. 2024, MNRAS, 531, 4857
Curtis-Lake, E., Carniani, S., Cameron, A., et al. 2023, NatAs, 7, 622
Daddi, E., Renzini, A., Pirzkal, N., et al. 2005, ApJ, 626, 680
Damjanov, I., McCarthy, P. J., Abraham, R. G., et al. 2009, ApJ, 695, 101
Davidzon, I., Ilbert, O., Laigle, C., et al. 2017, A&A, 605, A70
Dayal, P., Ferrara, A., Dunlop, J. S., & Pacucci, F. 2014, MNRAS, 445, 2545
de Graaff, A., Setton, D. J., Brammer, G., et al. 2025, NatAs, 9, 280
Donnan, C. T., McLeod, D. J., Dunlop, J. S., et al. 2023, MNRAS, 518, 6011
Donnan, C. T., McLure, R. J., Dunlop, J. S., et al. 2024, MNRAS, 533, 3222
Eisenstein, D. J., Willott, C., Alberts, S., et al. 2023, arXiv:2306.02465
Ellis, R. S., McLure, R. J., Dunlop, J. S., et al. 2013, ApJL, 763, L7
Elmegreen, B. G., & Elmegreen, D. M. 2005, ApJ, 627, 632
Endsley, R., Stark, D. P., Whitler, L., et al. 2023, MNRAS, 524, 2312
Ferreira, L., Adams, N., Conselice, C. J., et al. 2022, ApJL, 938, L2

Finkelstein, S. L., Bagley, M. B., Ferguson, H. C., et al. 2023, ApJL, 946, L13
Finkelstein, S. L., Bagley, M. B., Haro, P. A., et al. 2022, ApJL, 940, L55
Finkelstein, S. L., Leung, G. C. K., Bagley, M. B., et al. 2024, ApJL, 969, L2
Foreman-Mackey, D., Hogg, D. W., Lang, D., & Goodman, J. 2013, PASP, 125, 306
Förster Schreiber, N. M., Genzel, R., Bouché, N., et al. 2009, ApJ, 706, 1364
Franco, M., Akins, H. B., Casey, C. M., et al. 2024, ApJ, 973, 23
Fudamoto, Y., Inoue, A. K., & Sugahara, Y. 2022, ApJL, 938, L24
Fukugita, M., Ichikawa, T., Gunn, J. E., et al. 1996, AJ, 111, 1748
Gehrels, N. 1986, ApJ, 303, 336
Gelli, V., Mason, C., & Hayward, C. C. 2024, ApJ, 975, 192
Genzel, R., Newman, S., Jones, T., et al. 2011, ApJ, 733, 101
Glazebrook, K., Nanayakkara, T., Schreiber, C., et al. 2024, Natur, 628, 277
Glazebrook, K., Schreiber, C., Labbé, I., et al. 2017, Natur, 544, 71
Greene, J. E., Labbe, I., Goulding, A. D., et al. 2024, ApJ, 964, 39
Grogin, N. A., Kocevski, D. D., Faber, S. M., et al. 2011, ApJS, 197, 35
Guo, K., Zheng, X. Z., Wang, T., & Fu, H. 2015, ApJL, 808, L49
Hainline, K. N., Helton, J. M., Johnson, B. D., et al. 2024, ApJ, 964, 66
Hainline, K. N., Johnson, B. D., Robertson, B., et al. 2024, ApJ, 964, 71
Harikane, Y., Nakajima, K., Ouchi, M., et al. 2024, ApJ, 960, 56
Harikane, Y., Ouchi, M., Oguri, M., et al. 2023, ApJS, 265, 5
Harikane, Y., Zhang, Y., Nakajima, K., et al. 2023c, ApJ, 959, 39
Harris, C. R., Millman, K. J., van der Walt, S. J., et al. 2020, Natur, 585, 357
Holwerda, B. W., Bridge, J. S., Ryan, R., et al. 2018, A&A, 620, A132
Holwerda, B. W., Trenti, M., Clarkson, W., et al. 2014, ApJ, 788, 77
Illingworth, G. D., Magee, D., Oesch, P. A., et al. 2013, ApJS, 209, 6
Inami, H., Armus, L., Matsuhara, H., et al. 2018, A&A, 617, A130
Ishigaki, M., Kawamata, R., Ouchi, M., et al. 2018, ApJ, 854, 73
Ishikawa, Y., Morishita, T., Stiavelli, M., et al. 2022, ApJ, 936, 167
Ito, K., Valentino, F., Brammer, G., et al. 2024, ApJ, 964, 192
Jarosik, N., Bennett, C. L., Dunkley, J., et al. 2011, ApJS, 192, 14
Jung, I., Finkelstein, S. L., Larson, R. L., et al. 2022, arXiv:2212.09850
Kannan, R., Garaldi, E., Smith, A., et al. 2022, MNRAS, 511, 4005
Katz, H., Cameron, A. J., Saxena, A., et al. 2024, arXiv:2408.03189
Kocevski, D. D., Onoue, M., Inayoshi, K., et al. 2023, ApJL, 954, L4
Koekemoer, A. M., Faber, S. M., Ferguson, H. C., et al. 2011, ApJS, 197, 36
Kokubo, M., & Harikane, Y. 2024, arXiv:2407.04777
Kragh Jespersen, C., Steinhardt, C. L., Somerville, R. S., & Lovell, C. C. 2025, ApJ, 982, 23
Labbe, I., Greene, J. E., Bezanson, R., et al. 2025, ApJ, 978, 92
Larson, R. L., Finkelstein, S. L., Hutchison, T. A., et al. 2022, ApJ, 930, 104
Larson, R. L., Finkelstein, S. L., Kocevski, D. D., et al. 2023a, ApJL, 953, L29
Larson, R. L., Hutchison, T. A., Bagley, M., et al. 2023b, ApJ, 958, 141
Leethochawalit, N., Roberts-Borsani, G., Morishita, T., Trenti, M., & Treu, T. 2023a, MNRAS, 524, 5454
Leethochawalit, N., Trenti, M., Santini, P., et al. 2023b, ApJL, 942, L26
Leung, G. C. K., Bagley, M. B., Finkelstein, S. L., et al. 2023, ApJL, 954, L46
Livermore, R. C., Trenti, M., Bradley, L. D., et al. 2018, ApJL, 861, L17
Llerena, M., Amorìn, R., Pentericci, L., et al. 2024, A&A, 691, A59
Lovell, C. C., Harrison, I., Harikane, Y., Tacchella, S., & Wilkins, S. M. 2023, MNRAS, 518, 2511
Madau, P., Ferguson, H. C., Dickinson, M. E., et al. 1996, MNRAS, 283, 1388
Mashian, N., Oesch, P. A., & Loeb, A. 2016, MNRAS, 455, 2101
Mason, C. A., Trenti, M., & Treu, T. 2023, MNRAS, 521, 497
Mason, C. A., Treu, T., Schmidt, K. B., et al. 2015, ApJ, 805, 79
Matthee, J., Naidu, R. P., Brammer, G., et al. 2024, ApJ, 963, 129
McLeod, D. J., Donnan, C. T., McLure, R. J., et al. 2024, MNRAS, 527, 5004
Morishita, T. 2021, ApJS, 253, 4
Morishita, T. 2023, mtakahiro/bbpn: v1.3, Zenodo, doi:10.5281/zenodo.10067906
Morishita, T., Liu, Z., Stiavelli, M., et al. 2025a, ApJ, 982, 153
Morishita, T., Roberts-Borsani, G., Treu, T., et al. 2023, ApJL, 947, L24
Morishita, T., & Stiavelli, M. 2023, ApJL, 946, L35
Morishita, T., Stiavelli, M., Chary, R.-R., et al. 2024, ApJ, 963, 9
Morishita, T., Stiavelli, M., Trenti, M., et al. 2020, ApJ, 904, 50
Morishita, T., Stiavelli, M., Vanzella, E., et al. 2025b, arXiv:2501.11879
Morishita, T., Trenti, M., Stiavelli, M., et al. 2018, ApJ, 867, 150
Naidu, R. P., Oesch, P. A., Dokkum, P. V., et al. 2022, ApJL, 940, L14
Nanayakkara, T., Glazebrook, K., Jacobs, C., et al. 2024, NatSR, 14, 3724
Napolitano, L., Castellano, M., Pentericci, L., et al. 2025, A&A, 693, A50
Newman, A. B., Ellis, R. S., Andreon, S., et al. 2014, ApJ, 788, 51
Nonino, M., Glazebrook, K., Burgasser, A. J., et al. 2023, ApJL, 942, L29
Oesch, P. A., Bouwens, R. J., Illingworth, G. D., et al. 2010, ApJL, 709, L16
Oesch, P. A., Bouwens, R. J., Illingworth, G. D., et al. 2013, ApJ, 773, 75
Oesch, P. A., Bouwens, R. J., Illingworth, G. D., Labbé, I., & Stefanon, M. 2018, ApJ, 855, 105
Oke, J. B., & Gunn, J. E. 1983, ApJ, 266, 713
Onoue, M., Inayoshi, K., Ding, X., et al. 2023, ApJL, 942, L17
Pérez-González, P. G., Costantin, L., Langeroodi, D., et al. 2023, ApJL, 951, L1
Rayner, J. T., Toomey, D. W., Onaka, P. M., et al. 2003, PASP, 115, 362
Ren, K., Trenti, M., & Mason, C. A. 2019, ApJ, 878, 114
Rinaldi, P., Caputi, K. I., Costantin, L., et al. 2023, ApJ, 952, 143
Roberts-Borsani, G., Bagley, M., Rojas-Ruiz, S., et al. 2024a, arXiv:2407.17551
Roberts-Borsani, G., Morishita, T., Treu, T., Leethochawalit, N., & Trenti, M. 2022, ApJ, 927, 236
Roberts-Borsani, G., Treu, T., Shapley, A., et al. 2024b, ApJ, 976, 193
Roberts-Borsani, G. W., Bouwens, R. J., Oesch, P. A., et al. 2016, ApJ, 823, 143
Robertson, B. E. 2010, ApJL, 716, L229
Robertson, B., Johnson, B. D., Tacchella, S., et al. 2024, ApJ, 970, 31
Rojas-Ruiz, S., Bagley, M. B., Roberts-Borsani, G., et al. 2024, arXiv:2408.00843
Rojas-Ruiz, S., Finkelstein, S. L., Bagley, M. B., et al. 2020, ApJ, 891, 146
Ryan, R. E., Thorman, P. A., Yan, H., et al. 2011, ApJ, 739, 83
Schechter, P. 1976, ApJ, 203, 297
Schlafly, E. F., & Finkbeiner, D. P. 2011, ApJ, 737, 103
Schlegel, D. J., Finkbeiner, D. P., & Davis, M. 1998, ApJ, 500, 525
Schmidt, K. B., Treu, T., Brammer, G. B., et al. 2014, ApJL, 782, L36
Schneider, A. C., Burgasser, A. J., Gerasimov, R., et al. 2020, ApJ, 898, 77
Scholtz, J., Witten, C., Laporte, N., et al. 2024, A&A, 687, A283
Schreiber, C., Labbé, I., Glazebrook, K., et al. 2018, A&A, 611, A22
Setton, D. J., Verrico, M., Bezanson, R., et al. 2022, ApJ, 931, 51
Somerville, R. S., Lee, K., Ferguson, H. C., et al. 2004, ApJL, 600, L171
Stark, D. P., Ellis, R. S., Charlot, S., et al. 2017, MNRAS, 464, 469
Stefanon, M., Labbé, I., Bouwens, R. J., et al. 2019, ApJ, 883, 99
Steidel, C. C., Adelberger, K. L., Dickinson, M., et al. 1998, ApJ, 492, 428
Tacchella, S., Bose, S., Conroy, C., Eisenstein, D. J., & Johnson, B. D. 2018, ApJ, 868, 92
Tacchella, S., Eisenstein, D. J., Hainline, K., et al. 2023, ApJ, 952, 74
Tanaka, M., Onodera, M., Shimakawa, R., et al. 2024, ApJ, 970, 59
Tanaka, M., Valentino, F., Toft, S., et al. 2019, ApJL, 885, L34
Tang, M., Stark, D. P., Chen, Z., et al. 2023, MNRAS, 526, 1657
Tilvi, V., Malhotra, S., Rhoads, J. E., et al. 2020, ApJL, 891, L10
Trapp, A. C., & Furlanetto, S. R. 2020, MNRAS, 499, 2401
Trapp, A. C., Furlanetto, S. R., & Davies, F. B. 2023, MNRAS, 524, 5891
Trenti, M., Bradley, L. D., Stiavelli, M., et al. 2011, ApJL, 727, L39
Trenti, M., Bradley, L. D., Stiavelli, M., et al. 2012, ApJ, 746, 55
Trenti, M., & Stiavelli, M. 2008, ApJ, 676, 767
Treu, T., Roberts-Borsani, G., Bradac, M., et al. 2022, ApJ, 935, 110
Treu, T., Schmidt, K. B., Trenti, M., Bradley, L. D., & Stiavelli, M. 2013, ApJL, 775, L29
Übler, H., Maiolino, R., Curtis-Lake, E., et al. 2023, A&A, 677, A145
Valentino, F., Brammer, G., Gould, K. M. L., et al. 2023, ApJ, 947, 20
Valentino, F., Magdis, G. E., Daddi, E., et al. 2020, ApJ, 890, 24
van Dokkum, P. G. 2001, PASP, 113, 1420
Vanderplas, J., Connolly, A., Ivezić, Ž., & Gray, A. 2012, in Conf. on Intelligent Data Understanding (CIDU) (Piscataway, NJ: IEEE), 47
Vulcani, B., Trenti, M., Calvi, V., et al. 2017, ApJ, 836, 239
Vulcani, B., Treu, T., Calabrò, A., et al. 2023, ApJL, 948, L15
Wang, T., Sun, H., Zhou, L., et al. 2024, arXiv:2403.02399
Weaver, J. R., Davidzon, I., Toft, S., et al. 2023, A&A, 677, A184
Weibel, A., de Graaff, A., Setton, D. J., et al. 2024, arXiv:2409.03829
Whitler, L., Endsley, R., Stark, D. P., et al. 2023, MNRAS, 519, 157
Wilkins, S. M., Vijayan, A. P., Lovell, C. C., et al. 2023, MNRAS, 519, 3118
Williams, C. C., Curtis-Lake, E., Hainline, K. N., et al. 2018, ApJS, 236, 33
Williams, C. C., Oesch, P. A., Weibel, A., et al. 2025, ApJ, 979, 140
Williams, R. J., Quadri, R. F., Franx, M., van Dokkum, P., & Labbé, I. 2009, ApJ, 691, 1879
Willott, C. J., Desprez, G., Asada, Y., et al. 2024, ApJ, 966, 74
Witten, C., McClymont, W., Laporte, N., et al. 2025, MNRAS, 537, 112
Xiao, M., Williams, C. C., Oesch, P. A., et al. 2024, arXiv:2412.13264
Yan, H., Yan, L., Zamojski, M. A., et al. 2011, ApJL, 728, L22
Yung, L. Y. A., Somerville, R. S., Finkelstein, S. L., Popping, G., & Davé, R. 2019, MNRAS, 483, 2983
Zhang, Z., Jiang, L., Liu, W., & Ho, L. C. 2024, arXiv:2411.02729